PRESSURIZED EXPULSION OF NONISOTHERMAL

SINGLE-PHASE CRYOGEN

Clifford K. Forester
Research Engineer
The Boeing Company
Seattle, Washington

The performance of single-phase storage and expulsion systems is strongly affected by temperature variations within the stored cryogen which are generated during heat transfer. Peculiar operating responses are indicated by spontaneous changes in fluid pressure which accompany "g" level changes, increased heater surface temperature, and durations of pressure cycles which differ considerably from that which is computed for an isothermal cryogen. The nonisothermal characteristics are predicted with a numerical model which includes the simultaneous solution of the time dependent conservation equations of mass, energy, and momentum in two space dimensions of Cartesian coordinates for boundary conditions which approximate those of the flight cryogenic system. The methodology of the numerical method and some comparisons between the predictions and the Apollo 12 flight data are included.

Acknowledgement

Table of Contents

Illustrations

Nomenclature

$\dot{P}_g$ Time derivative of the global pressure

P_g Global pressure

P Pressure

ρ Mass density

ρ_c Average mass density of the fluid in the container

ρ_p Mass density of fluid in the external plumbing

h Enthalpy

e Specific internal energy

T Temperature

k Thermal conductivity

μ Kinematic viscosity

g_x x- direction acceleration component

u x- direction velocity

A_x Cross sectional area of a cell face normal to the x- direction

Δx x-direction discrete distance

X x- direction mass rate

HX Discrete stress tensor, momentum convection and body force terms of the x-momentum equation

g_y y- direction acceleration component

v y- direction velocity

Y	y- direction mass rate
Δy	y- direction discrete distance
A_y	Cross sectional area of a cell face normal to the y- direction
HY	Discrete stress tensor, momentum convection, and body force terms of the y- momentum equation
θ	$\equiv (- \rho \, \partial h / \partial \rho)\vert_p$
ϕ	$\equiv (1/\rho \ \partial p / \partial e)\vert_\rho$
V	Cell volume
V_c	Container volume
V_p	Volume of the external plumbing
Δt	Time increment
δ	A fraction of a time increment
EF	Container elastic factor
HCX	Thermal capacitance of a material located at a cell face
TWX	Temperature of a cell face
$\dot{Q}X$	The prescribed cell face heating rate
g	The magnitude of g acceleration vector
Q_{DA}	The adiabatic heat deficiency of a nonisothermal fluid system
Q_{DT}	The heat deficiency of a process in which a discrete amount of heat is added during the process

$\Delta P \big|_{max}$ The pressure decay potential of a nonisothermal fluid system

Z   Compressibility

M   Mass

$\dot{m}$ Mass rate

n   The inverse of the polytropic exponent

References

1. Forester, C. K., "Numerical Integration of Conservation Equations for the Storage and Expulsion of Single-Phase Cryogen", M.S. Thesis, University of Washington, Seattle, Washington, 1969.

2. Forester, C. K., and Emery, A. F., "The Numerical Computation of the Free Convection of Cryogens with Variable Density", to be published.

3. Williams, G. P., "Numerical Integration of the Three-Dimensional Navier-Stokes Equations for Incompressible Flow", J. Fluid Mechanics, Vol. 37, Part 4, pp. 727-750, 1969.

4. Harlow, Francis H. and Welch, J. E., "Numerical Calculation of Time-Dependent Viscous Incompressible Flow of Fluid with a Free Surface", Physics of Fluids, No. 12, Vol. 8, 1965.

PRESSURIZED EXPULSION OF NONISOTHERMAL

SINGLE-PHASE CRYOGEN

Clifford K. Forester
Research Engineer
The Boeing Company
Seattle, Washington

The single-phase storage concept has been employed in the design of the Gemini and Apollo atmosphere and fuel cell supply equipment. In the course of using these systems, some peculiar performance characteristics have been observed during flight operations. For example, shortly after the launch of Gemini II and Apollo 12, abrupt decreases in the oxygen storage pressure in excess of 100 psi have been noted. Additionally, the observed time required to complete a pressurization cycle has been both substantially shorter and longer than the duration predicted from calculations which assume the stored cryogen is isothermal.

In this paper, the methodology of a numerical model is presented which, for the comparisons this far made with Apollo 12 and 14 flight data, appears to predict the observed peculiarities. Several considerations comprise the numerical model:

1) the methodology of the General Elliptic Method - GEM

2) the 1/2 box model in which the GEM is applied

3) the method of accounting for the cryogenic container elasticity

4) the method of treating the gas trapped in the external volume

The first two of these are discussed in order after the introduction. The mathematical derivation of the last two are provided in Appendix A. These considerations are followed by a discussion of the physical characteristics of

the Apollo oxygen system and a brief discussion of the
flight data reduction considerations. Finally, a discus-
sion is provided in which the comparison between Apollo 12
flight data and the 1/2 box model predictions for two pro-
blems is presented.

The Methodology of the General Elliptic Method (GEM)

Because of the length, no attempt is provided here to docu-
ment the literature now available on numerical algorithms
which model the conservation equations of mass, energy, and
momentum in time and space. A review of this literature
at the end of 1967 showed that the methods generally ap-
plied either to incompressible flow or high speed compres-
sible flow. These algorithms are restrictive enough so
that they eliminate from practical analysis one of the
most intriging aspects of the problems at hand which is to
compute the cryogen pressure history. As a result, a new
algorithm, the General Elliptic Method (GEM), was developed
by the author as a part-time effort and was documented in
reference (1). Reference (2) includes a literature survey
of those algorithms which depend upon an elliptical equa-
tion and some refinements of the GEM which was presented
in reference (1). However, the GEM had to be modified to
suit the special requirements which the problems at hand
establish. Since these modifications are an intricate
part of the computational method, a complete description
of the methodology is necessary and is illustrated subse-
quently.

The conservation equations of mass, energy, and momentum for a Newtonian fluid may be written in the x- and y-directions of Cartesian coordinates respectively as

$$\frac{\partial \rho}{\partial t} + \frac{\partial(\rho u)}{\partial x} + \frac{\partial(\rho v)}{\partial y} = 0$$

$$\frac{\partial(\rho e)}{\partial t} + \frac{\partial(\rho u h)}{\partial x} + \frac{\partial(\rho v h)}{\partial y} = \frac{\partial}{\partial x}\left(k\frac{\partial T}{\partial x}\right) + \frac{\partial}{\partial y}\left(k\frac{\partial T}{\partial y}\right)$$

$$\frac{\partial(\rho u)}{\partial t} + \frac{\partial(\rho u^2)}{\partial x} + \frac{\partial(\rho v u)}{\partial y} + \frac{\partial P}{\partial x} + g_x \rho = \sigma_x$$

$$\frac{\partial(\rho v)}{\partial t} + \frac{\partial(\rho v^2)}{\partial y} + \frac{\partial(\rho u v)}{\partial x} + \frac{\partial P}{\partial y} + g_y \rho = \sigma_y$$

where

$$\sigma_x = \frac{\partial}{\partial x}\left[2\mu\frac{\partial u}{\partial x} - \frac{2}{3}\mu\left(\frac{\partial u}{\partial x} + \frac{\partial v}{\partial y}\right)\right] + \frac{\partial}{\partial y}\left[\mu\left(\frac{\partial u}{\partial y} + \frac{\partial v}{\partial x}\right)\right]$$

$$\sigma_y = \frac{\partial}{\partial y}\left[2\mu\frac{\partial v}{\partial y} - \frac{2}{3}\mu\left(\frac{\partial u}{\partial x} + \frac{\partial v}{\partial y}\right)\right] + \frac{\partial}{\partial x}\left[\mu\left(\frac{\partial v}{\partial x} + \frac{\partial u}{\partial y}\right)\right] \qquad (1)$$

and where ρ is the mass density, u is the x-direction velocity, v is the y- direction velocity, e is the specific internal energy, h is the enthalpy, k is the thermal conductivity, T is the temperature, P is the pressure, g_x is the x- direction acceleration component, g_y is the y-direction acceleration component, and μ is the kinematic viscosity.

Since
$$e = e(P, \rho) \quad \text{and} \quad h \equiv e + P/\rho$$

$$\frac{\partial(\rho e)}{\partial t} = \frac{1}{\phi}\frac{\partial P}{\partial t} + (h - \theta)\frac{\partial \rho}{\partial t} \qquad (2)$$

where
$$\phi \equiv \frac{1}{\rho}\left.\frac{\partial P}{\partial e}\right|_\rho$$

and
$$\theta \equiv -\rho\left.\frac{\partial h}{\partial \rho}\right|_P$$

and the product of ϕ and θ ($\phi\theta$) is the speed of sound squared of the fluid.

55

Because the Mach number is less than about 10^{-3} for the problems to be considered, only pressure waves of the acoustic variety will dominate during the various flow processes of interest. But since, for the purposes here, modeling acoustic waves is unnecessary, and since each acoustic wave only subtly modifies the density field as it passes by any point of interest, the local time derivative of pressure ($\partial P/\partial t$) may be replaced with the time derivative of the global pressure (P_g) or ($\partial P_g/\partial t) \rightarrow \dot{P}_g$. (Note however that this simplification does not eliminate spatial gradients of pressure from the momentum equations.) Thus equation (2) may be simplified to read

$$\frac{\partial(\rho e)}{\partial t} = \frac{\dot{P}_g}{\phi} + (h - \theta)\frac{\partial \rho}{\partial t} \tag{3}$$

Now the mass rates which pass normal to and through the center of the sides of a cell are defined as

$$X \equiv \rho u A_\chi \text{ and } Y \equiv \rho v A_y \tag{4}$$

where A_x and A_y are the areas of the cell faces perpendicular to the x and y axes respectively. Equations (1, 3 and 4) can be combined as

$$\frac{\partial \rho}{\partial t} + \frac{1}{A_\chi}\frac{\partial X}{\partial x} + \frac{1}{A_y}\frac{\partial Y}{\partial y} = 0 \tag{5a}$$

$$\frac{\dot{P}_g}{\phi} = (h-\theta)\left[\frac{1}{A_\chi}\frac{\partial X}{\partial x} + \frac{1}{A_y}\frac{\partial Y}{\partial y}\right] - \left[\frac{1}{A_\chi}\frac{\partial(Xh)}{\partial x}\right] - \left[\frac{1}{A_y}\frac{\partial(Yh)}{\partial y}\right] + \left[\frac{1}{A_\chi}\frac{\partial}{\partial x}(kA_\chi\frac{\partial T}{\partial x})\right] + \left[\frac{1}{A_y}\frac{\partial}{\partial y}(kA_y\frac{\partial T}{\partial y})\right] \tag{5b}$$

$$\frac{\partial X}{\partial t} + \frac{\partial(Xu)}{\partial x} + \frac{A_\chi}{A_y}\frac{\partial Yu}{\partial y} + A_\chi\frac{\partial P}{\partial x} + \mathscr{B}_\chi A_\chi \rho = A_\chi \sigma_\chi \tag{5c}$$

$$\frac{\partial Y}{\partial t} + \frac{\partial(Yv)}{\partial y} + \frac{A_y}{A_\chi}\frac{\partial(Xv)}{\partial x} + A_y\frac{\partial P}{\partial y} + \mathscr{B}_y A_y \rho = A_y \sigma_y \tag{5d}$$

Now (5a) – (5d) are transformed into a discrete set of simultaneous algebraic equations with the use of a discrete grid network.

It should be noted that two types of grid networks are in general use:

1) a mathematical grid in which <u>all</u> dependent variables are defined at common points and

2) a physical grid in which the state and transport properties are defined in the centers of control volumes and the velocities are defined normal to and in the center of the faces which bound the volumes.

The physical grid possesses three important advantages:

1) a unique definition of local mass conservation is specified.

2) The resolution of thermal and velocity boundary layers are improved for the same grid density since the temperature and velocity points are $\Delta x/2$ or $\Delta y/2$ from solid boundaries rather than the usual Δx or Δy for the mathematical grid. This is achieved without the usual complication that nonlinear grid spacings involve.

3) The procedures for treating mathematical singularities (e.g., the center of a polar coordinate system) are not ambiguous.

For these reasons the physical grid is employed in the following discrete formulation. Figure (1) shows a typical computational cell which is imbedded in an array of such cells which altogether comprise the volume of the entire region of interest. For identification purposes, the subscripts i and j are used with the cell center variables P, ρ, T, h, e, k, and μ to denote their relative location in the complete cellular array. The whole integers, i and j, are counted with the increasing x- and y- directions, respectively. The velocities and mass rates which are defined at the cell sides are denoted by half integers and are counted similarly to the cell center values. Both the integer and half integer nodal points are defined to be separated by a cell width (Δx) and a cell height (Δy).

The difference approximations of equations (5a) – (5d) for a uniform two dimensional rectangular grid with an arbitrary depth in the third dimension, are

$$\rho_{ij}^{t+1} = \rho_{ij}^{t} + D_{ij}^{t+1} \frac{\Delta t}{V} \tag{6a}$$

$$\left.\begin{array}{l} \dot{P}_{\!\beta} = \theta_{ij}^{t+\delta} (E_{ij}^{t+\delta} + \phi_{ij}^{t+\delta} D_{ij}^{t+1}) \frac{\Delta t}{V} \\[2em] P_{\!\beta}^{t+1} = P_{\!\beta}^{t} + \dot{P}_{\!\beta} \Delta t \end{array}\right\} \text{ energy equation} \begin{array}{l} \\[1em] (6b) \\[2em] (6c) \end{array}$$

$$X_{i+\frac{1}{2}j}^{t+1} = X_{i+\frac{1}{2}j}^{t} + A_x \left[\left(\frac{P_{ij}-P_{i+1j}}{\Delta x}\right)^{t+1} + HX_{i+\frac{1}{2}j}^{t} \right] \Delta t \tag{6d}$$

$$Y_{ij+\frac{1}{2}}^{t+1} = Y_{ij+\frac{1}{2}}^{t} + A_y \left[\left(\frac{P_{ij}-P_{ij+1}}{\Delta y}\right)^{t+1} + HY_{ij+\frac{1}{2}}^{t} \right] \Delta t \tag{6e}$$

where

$$D_{ij}^{t+1} \equiv \left(X_{i-\frac{1}{2}j} - X_{i+\frac{1}{2}j} + Y_{ij-\frac{1}{2}} - Y_{ij+\frac{1}{2}} \right)^{t+1}$$

and $V = A_x \Delta x = A_y \Delta y$ (the cell volume) and the superscripts $t + 1$ and $t + \delta$ indicate an evaluation at the time $t + \Delta t$ and $t + \delta$ (Δt) respectively ($\delta = 1/2, 0$). For $\delta = 1/2$, ϕ_{ij}, θ_{ij}, $\dot{P}_g$ and the terms of the convection of heat are nearly time centered. Such an alternative has certain advantages which are provided together with the methodology for implementation in reference (2).

D_{ij} is the net added mass rate to an ij cell, E_{ij} is the net added heat rate to an ij cell by conduction and convection. $HX_{i+1/2j}$ and $HY_{ij+1/2}$ are the viscous, body force and the convection terms of momentum in the x- and y- directions respectively. The difference expressions for these terms are given in references (1) and (2) and are omitted because they are not essential to the illustration of the methodology of the GEM.

58

(6b) may be revised as

$$D_{ij}^{t+1} = \dot{P}_{g} \frac{V}{(\phi\theta)_{ij}^{t}} - (\frac{E}{\theta})_{ij}^{t} \tag{7}$$

Since D_{ij}^{t+1} summed over the total volume is equal to net mass rate inflow at the boundaries, and since $\dot{P}_{g}$ is a constant over the total volume, (7) may be integrated over the total volume to yield

$$\dot{P}_{g} = \frac{\sum(\frac{E}{\theta})_{ij}^{t} - \binom{\text{net mass rate outflow}}{\text{at the boundaries}}}{\sum(\frac{V}{\phi\theta})_{ij}^{t}} \tag{8}$$

where $\sum$ is the sum over all active cells.

Now (6a) and (7) may be combined to form

$$\rho_{ij}^{t+1} = \rho_{ij}^{t} + \frac{\Delta t}{V}\left[\frac{\dot{P}_{g}V}{(\phi\theta)_{ij}} - (\frac{E}{\theta})_{ij}^{t}\right] \tag{9}$$

Equations (6c, 8, and 9) apply only to a container whose walls are rigid. These equations may be modified in two ways to accomodate the elasticity effect of the container wall and the external volume. The first method involves simply the multiplication of (8) by (EF) where

$$EF = \frac{1}{1 + (\rho\phi\theta)_{c}\,(ESF)}$$

where

$$ESF \equiv \left[\frac{3r(1-\sigma)}{2bE} + \frac{V_{p}}{V_{c}}\,\frac{n}{P_{g}}\,\frac{\rho_{p}}{\rho_{c}}\right] \tag{10}$$

which is the elastic factor derived in Appendix A. $(\rho\phi\theta)_{c}$ is evaluated at the average stored fluid density. $(\rho V)_{p}$ is the product of the external plumbing volume and the density of the fluid in the volume. n is the inverse of the polytropic coefficient and is unity for an isothermal process. This method of modifying $\dot{P}_{g}$ for the elastic effect is valid provided the ratio of the volume occupied by the thermal boundary layer to the total volume is small.

59

A general method of incorporating the elastic factor in-
volves modifying (8) as

$$\dot{P}_\beta = \frac{\sum (\frac{E}{\theta})_{ij}^t - \binom{\text{net mass rate outflow}}{\text{at the boundaries}}}{V \sum \left[(\frac{1}{\phi \theta})_{ij}^t + \rho_{ij}^t \text{ (ESF)} \right]} \tag{11}$$

and (9) may be modified as

$$\rho_{ij}^t = \rho_{ij}^t - \frac{\Delta t}{V} HH_{ij} \tag{12}$$

where

$$HH_{ij} \equiv \left\{ (\frac{E}{\theta})_{ij}^t - V\dot{P}_\beta \left[(\frac{1}{\phi \theta})_{ij}^t + \rho_{ij} \text{ (ESF)} \right] \right\}$$

For convenience, equation (6c) is renumbered as

$$P_\beta^{t+1} = P_\beta^t + \Delta t (\dot{P}_\beta) \tag{13}$$

Equations (11, 12, and 13) are the discrete conservation
equations of mass and energy which must be solved simul-
taneously with the momentum balances (6d) and (6e). To
implement this, equations (6d and 6e) are discretely dif-
ferentiated with respect to x and y respectively and com-
bine to form

$$D_{ij}^{t+1} = D_{ij}^t + \Delta t (PI2_{ij}^{t+1} - HI2_{ij}^t) \tag{14}$$

where

$$PI2_{ij}^{t+1} = \frac{A_x}{\Delta x} (P_{i-1,j} - 2P_{ij} + P_{i+1,j})^{t+1} + \frac{A_y}{\Delta y} (P_{i,j-1} - 2P_{ij} + P_{i,j+1})^{t+1}$$

and

$$HI2_{ij}^t \equiv HX_{i-\frac{1}{2},j}^t - HX_{i+\frac{1}{2},j}^t + HY_{i,j-\frac{1}{2}}^t - HY_{i,j+\frac{1}{2}}^t$$

The D_{ij}^{t+1} term is eliminated from (14) with the aid of (6a)
and (12) to yield

$$0 = D_{ij}^t + HH_{ij}^t + \Delta t (PI2_{ij}^{t+1} - HI2_{ij}^t) \tag{15}$$

Equation (15) is an elliptic difference equation which may be solved by direct inversion, direct Fourier methods (see reference 3), and iterative methods. For generality and simplicity, the Liebmann iterative method is employed which is used in the MAC method of Harlow and Welch (reference 4). NIP is defined as the number of iterations used to solve equation (15). The pressures which result from the approximate solution of (15) are used in the momentum balances to obtain updated x- and y- direction mass rates in the active cells. With the use of the thermodynamic relations, the updated values of density and global pressure from equations (12 and 13) are used to find updated values of temperature, enthalpy, thermal conductivity, viscosity, θ and ϕ for all active cells.

The sequence of computations for the General Elliptic Method (GEM) is summarized as:

1) Prescribe the initial values of the mass rates $(X_{i+1/2j}, Y_{ij+1/2})$, the global pressure (P_g), and the density (ρ_{ij}) for all active cells including the border values. Compute the velocities $(u_{ij}$ and $v_{ij})$ for all the field and border locations using the mass rate definitions. Evaluate the exterior velocities for the no-slip and free-slip conditions. Find $T_{ij}, h_{ij}, k_{ij}, \mu_{ij}, (\theta\phi)_{ij}$, and θ_{ij} with P_g and ρ_{ij} from the thermodynamic and transport relations. These relations may be defined in terms of equations of state or tabular data. For the simulations reported, the thermodynamic properties are tabulated at three pressure levels; 850 psia, 900 psia, and 950 psia. Linear interpolation with density and pressure are used to find the other desired thermodynamic properties. The transport properties are determined from a linear interpolation with temperature in single arrays of thermal conductivity and viscosity at 900 psia.

2) Evaluate $HX_{i+1/2j}$, $HY_{ij+1/2}$, E_{ij}, D_{ij}, (EF), $\dot{P}_g$ and HH_{ij} for all active cells from the existing field values.

3) Compute ρ^{t+1}_{ij} and P_g^{t+1} from (12) and (13). With these values find T^{t+1}_{ij}, h^{t+1}_{ij}, k^{t+1}_{ij}, μ^{t+1}_{ij}, $(\theta\phi)^{t+1}_{ij}$, and θ^{t+1}_{ij} from the linear table searches. Compute the border values of $X^{t+1}_{i+1/2\,j}$ and $Y^{t+1}_{ij+1/2}$ from the expulsion rate function.

4) Solve (15) approximately with NIP iterations for P^{t+1}_{ij} for all cells inside the border and immediately outside the border. The pressure P_{ij} in cells outside and adjoining the border are obtained directly from the momentum balances (6d) and (6e) and are recomputed each sweep of the field for new tentative values. Note that the border values of $HX_{i+1/2\,j}$ and $HY_{ij+1/2}$ used in (15), (6d), and (6e) must be the same but may be any desired value. It is best to set these to zero.

5) Use the values of pressure (P_{ij}) from step 4 in (6d) and (6e) to obtain the remaining unknown values of $X^{t+1}_{i+1/2\,j}$ and $Y^{t+1}_{ij+1/2}$ respectively.

6) The updated values then become the current values at time (t) and step 2 through step 5 may be repeated until the time (t) has been advanced to some value of interest.

Some discussion is now devoted to the various boundary conditions which are required to define all derivatives and quantities normal to the boundary. All mass rates normal to the border must be set to zero except where expulsion is specified. The velocities are computed from the mass rates, the normal cross sectional area through which the mass flows, and the average density of respective adjoining cells. Where mass rates are nonzero at the border, the velocity calculation requires a prescription of the density in the external receiver cell and is set equal to that in the supplier cell. This velocity enters into two viscous terms. Two other viscous terms require the prescription of velocities parallel to the boundary in all external cells. Where no-slip boundaries are required, the external

velocity is set equal and opposite to the values in the active adjoining cell. Where free-slip boundary velocities are required, the external velocity is set equal to the values in the active adjoining cell. These velocities in external cells are computed _after_ all the velocities have been computed which reside inside and on the border. The $HX_{i+1/2j}$ and $HY_{ij+1/2}$ terms required by the momentum balances on the border may be set to any value but for convenience are set to zero. This follows from the fact that since the mass rates at t+1 and t are prescribed on the border, the momentum balances are not required to generate these values at the border . For these to balance then it is only necessary that the values of $HX_{i+1/2j}$ and $HY_{ij+1/2}$ defined on the border which are used in the elliptic equation (15) be the same as those used in the border momentum balances to find the unknown external cell pressure which is required by equation (15) during the iterative solution.

The heat conduction terms involve gradients of temperature normal to the sides of a cell. Cell sides at which the heat rate is prescribed may be used to calculate these gradients. For generality, it is assumed that any cell face at which the heating rate is prescribed has an arbitrary thermal capacitance. The cell face temperature is determined with an implicit energy balance on a cell face of interest and for a left cell face is

$$\overset{\bullet}{Q}X_{i-\frac{1}{2}j}^{t} = \frac{(TWX_{i-\frac{1}{2}j}^{t+1} - TWX_{i-\frac{1}{2}j}^{t})(HCX_{i-\frac{1}{2}j})^{t}}{\Delta t}$$

$$+ (TWX_{i-\frac{1}{2}j}^{t+1} - T_{ij}^{t})(k_{i-\frac{1}{2}j} + k_{ij})^{t} \frac{A_{X}}{\Delta X} \qquad (16)$$

where $\overset{\bullet}{Q}X_{i+1/2j}$ is the prescribed cell face heat rate, $HCX_{i=1/2j}$ is the cell face thermal capacitance, $TWX_{i-1/2j}$ is the face temperature, $k_{i-1/2j}$ is the thermal conductivity at temperature $TWX_{i-1/2j}$ and T_{ij} is the cell temperature. Equation (6) may be solved for the unknown

$TWX_{i-1/2j}^{t+1}$ by algebraic manipulation and yields

$$TWX_{i-\frac{1}{2}j}^{t+1} = \frac{\dot{Q}X_{i-\frac{1}{2}j}^{t} + T_{ij}^{t}(k_{i-\frac{1}{2}j}+k_{ij})^{t}(\frac{A_x}{\Delta x}) + TWX_{i-\frac{1}{2}j}^{t}\frac{HCX_{i-\frac{1}{2}j}}{\Delta t}}{\frac{HCX}{\Delta t}_{i-\frac{1}{2}j}^{t} + (k_{i-\frac{1}{2}j}+k_{ij})(\frac{A_x}{\Delta x})} \qquad (17)$$

Similar expressions to equation (17) may be written for any other of the remaining cell faces. It should be noted that if (16) were not implicit in the heat conduction term, the time step would be restricted to

$$\Delta t \leqslant \frac{HCX_{i-\frac{1}{2}j}}{\frac{A_x}{\Delta x}(k_{i-\frac{1}{2}j}+k_{ij})} \qquad (18)$$

which could be substantially more restrictive than that required by GEM. (A discussion of GEM stability conditions is given below). Since the computational efficiency of the algorithm is directly related to Δt, equation (18) could impose severe increases in computing time. This is especially important since practical problems frequently require hours of computer time. For this reason, equation (17) is a preferred form over the explicit alternatives. This situation offers a fine example of the reason why implicit schemes are preferred or essential compared to explicit schemes whether the model of the boundary conditions or the field conservation equations are concerned. Reference (2) has some additional details with regard to explicit modeling of the conservation equations.

Note that for $HCX_{i-1/2j}$ and $\dot{Q}X_{i-1/2j}$ equal to zero, equation (17) reduces to $TWX_{i-1/2j}^{t+1} = T_{ij}^{t}$ which is the boundary condition for an ideally insulated cell face. Where the biased differences for the convective terms, reference (2), are employed, the fundamental stability conditions for GEM are:

$$\frac{1}{\Delta t_1} > (1+\phi)_{MAX}\left[2(A)(\frac{B+1}{\Delta x^2}+\frac{C+1}{\Delta y^2}) + (\frac{u}{\Delta x}, \frac{v}{\Delta y})_{MAX}\right] \qquad (19)$$

where

$A = (k/\rho cp)_{max}$

$B = 0, 1, 2$ for the x- direction, and

64

C = 0, 1, 2 for the y-direction
and

$$\frac{1}{\Delta t} \geqslant \left[2 \left(\frac{\mu}{\rho}\right)_{MAX} \left(\frac{1}{\Delta x^2} + \frac{1}{\Delta y^2}\right) + \left(\frac{u}{\Delta x}, \frac{v}{\Delta y}\right)_{MAX} \right] \tag{20}$$

B and C depend upon the number of cell faces which have prescribed heat rates in equation (19). For "g" spikes,

$$\Delta t_3 \leqslant \sqrt{\frac{(\Delta x, \Delta y)_{MIN}}{2B}} \tag{21}$$

is used to insure that equations (19) and (20) are nearly satisfied during a "g" spike. For time integration accuracy, equation (21) is modified to read

$$\Delta t_4 = 0.03 \sqrt{\frac{(\Delta x, \Delta y)}{B}} \tag{22}$$

In the calculations, equations (19) and (20) multiplied by about a factor of 1.5 in order to ensure small truncation errors in time while the "g" level is constant. Equations (19) and (20) are additionally superceded by the conditions
If $\dot{P}_g > 0$

then

$$\Delta t = \text{Min.} \ (\ \Delta t_1, \ \Delta t_2, \ 30) \tag{23a}$$

If $\Delta t > 1.3 \ \Delta t^{t-1/2}$

then

$$\Delta t = 1.3 \Delta t^{t-1/2} \tag{23b}$$

where

$\Delta t^{t-1/2}$ is the previous time step in seconds.

Equation (23a) has a thirty second value shown. It is used to minimize the truncation errors in time for pressurization strokes which are about four minutes long and which are simulated with coarse meshes.

Equation (23b) is used to limit the rate change of time step increases in order to promote time integration accuracy especially after "g" spikes or abrupt changes in the heating rate.

65

If there is a "g" spike, then

$$\Delta t = \text{Min} (\Delta t, \Delta t_4) \tag{23c}$$

is imposed for ten time steps.

There are a number of integral relations which provide checks on the accuracy or correctness of the various local calculations and these are now discussed. The sum over the volume of the local heat conduction terms should equal the prescribed boundary heating rate. The sum over the volume of the local convection of energy or momentum terms should equal the boundary values. The sum of the cell densities divided by the total number of cells should equal the average density computed from the initial density and the time integral of the mass density loss due to fluid expulsion. The change in global fluid pressure should equal the potential pressure decay when the non-isothermal cryogen is adiabatically restored to an isothermal state. The adiabatic potential pressure decay is defined algebraically as

$$\Delta P\big|_{MAX} = \frac{\phi \bar{\rho}}{V_C} Q_{DA} (EF) \tag{24}$$

$$Q_{DA} \equiv - \sum v \left[(\rho e)_{\bar{\rho}, P_B} - (\rho e)_{ij} \right]$$

where $\phi_{\bar{\rho}}$ is ϕ at the average density and initial pressure, V is the cell volume, V_C is the container volume, (EF) is the elastic factor of the system, Q_{DA} is the adiabatic heat deficiency, $(\rho e)_{\bar{\rho}, P_g}$ is the product of the average density and the specific internal energy which is evaluated at the average density and initial global pressure, and $(\rho e)_{ij}$ is the product of the cell density and specific internal energy. The validity of equation (24) is predicated upon the invariance of ϕ over the pressure change $(\Delta P\big|_{max})$.

Single-phase helium, parahydrogen, nitrogen, and oxygen in the density region from about the solid density through the low gas density exhibit a very weak or no dependency of ϕ upon P_g at any given density. Thus, equation (24) is a

66

simple means of computing the adiabatic potential pressure decay. Where tank wall or heater tube, thermal capacitance is involved, and/or where boundary heating is prescribed, a pressure decay however abrupt may not be adiabatic. If the end state temperatures of the metal are known, the energy added to the system can be computed and for such a condition equation (24) may be modified as

$$\Delta P\big|_{MAX} = \frac{\phi_{\bar{\rho}}\ Q_{DT}}{V_C}\ (\mathcal{C}F)$$

$$Q_{DT} \equiv -\sum V\left[(\rho e)_{\bar{\rho},P_{\mathcal{B}}} - (\rho e)_{ij}\right] - Q_B - Q_M \qquad (25)$$

where Q_B is the total boundary heating and Q_M is the total energy from the metal for any _short_ interval of time. _Short_ here is taken to mean a time period in which the change of $\bar{\rho}$ is small enough so that the desired accuracy of equation (25) is maintained during the event.

If the GEM is properly coded, all of the integral relations are satisfied exactly except for the energy convection terms which have a small nonconservative error. There is also a time dependent truncation error. In spite of these errors, the integral equation (24) and (25) are very nearly satisfied during time dependent calculations which is shown in an example in the results section.

The 1/2 Box Model

In order to simulate a physical problem with the GEM certain boundary and initial conditions must be established. Figure (2a) shows a sketch of the cross section of a flight oxygen tank in the plane of the "g" vector which is taken to be perpendicular to the heater tube. Figure (2b) shows a sketch of the geometry used for the numerical model. The region shown has a depth dimension so that the walls of the model form a box. The left wall is assumed to be a plane of symmetry in order to reduce the total volume of region of interest by two. (This reduces the computer time by a factor of two). For this reason, the model is called the 1/2 box model. Only one half the values of the container volume, heat input, expulsion rate, the heater tube

thermal capacitance (HTC), and plumbing volume are used in the calculations. The boundary conditions for the 1/2 box model are

1) freeslip left wall except where the heater element is

2) no-slip right, top, bottom and heater surfaces

3) uniform heat flux at the top, right and bottom wall for the heat leak simulation

4) insulated left wall except where the heater surface is

5) a flat plate heater surface midway up to the left wall, parallel to the left wall and extending the distance of the depth dimension

The initial conditions for the velocity and temperature fields, the global pressure, and the initial density, are chosen to be as consistent as possible with the conditions in the flight hardware for each simulation. All but the first two conditions are usually known accurately. Special measures must be taken to estimate these two initial conditions and these are discussed in the results section.

The Physical Description of the Apollo

Single-Phase Oxygen System

Figure (3) shows a schematic of an Apollo single-phase oxygen storage and supply system. The oxygen storage container is essentially a thin wall pressure vessel covered by a super insulation system. The container is vented and filled through pipes which are imbedded inside the super insulation for some distance before penetrating either the inner or outer container shells. On leaving the container, these pipes pass to the space craft surface. They are only active during the preflight oxygen loading procedures and then are sealed off shortly before the flight. A third line is attached to the tank and supplies oxygen

to the fuel cell regulator and the surge tank. The function of the surge tank is to separate the crew compartment from the low temperature cryogen and provide a large source of ambient gas ready for use at any time.

Inside the oxygen container are mounted two perforated tubes. One tube is a quantity gauge. The other tube is an extended surface for heat transfer. Several electrical resistance heater elements are helically wound around and welded to the heater tube. The control of the electrical power to the heating elements is accomplished by switches which are activated by fluid pressure. If the pressure falls below about 860 psia, the electrical power is engaged. If the pressure rises above about 900 psia, the electrical power is disengaged. Prior to Apollo 14, two fans were installed in the heater tube, one in each end. When operating, these fans draw oxygen through holes in the center of the heater tube assembly and ejected it radially at the ends, thereby stimulating circulating of the bulk of the stored cryogen. These fluid motions are potent enough to eliminate significant fluid temperature variations which are induced by heat transfer. As a result, the pressure history of the stored cryogen may be predicted by equations (A10) and A11). If the fans are not operated, the detail fluid motions in the container oxygen must be modelled in order to predict the pressure history. Successful modeling however, depends upon the prediction of the time variant "g" level, expulsion rate, and heat input. The method of determining each of these is now presented.

Reduction of Apollo Flight Data

It is the purpose of this discussion to provide some understanding of the considerations which are made in determining the "g" level, oxygen flow rate, and heat input histories as a function of the average stored oxygen density.

Figure (4a) shows a sketch of the space craft in relation to the roll, pitch and yaw axis and the earth. For simplicity the moon is not shown. Also shown in Figure (4b) is

a cross section of the space craft perpendicular to the roll axis and through the two Apollo 12 oxygen tanks. The heater tube in each tank is parallel to the roll axis. The "g" level and direction is defined if the inertial space acceleration vector can be evaluated. The method of rigid body dynamics is used to calculate the history of this vector. The angular rotation rates are taken directly from the Digital Auto Pilot (DAP) data. The angular acceleration is obtained by numerical differentiation of the rotation rates. When DAP data are not available, rotation and acceleration vectors are obtained by successive differentiation of the gyroscopic gimbal angles. The calculations showed that the accelerations induced by the solar pressure and the solar wind are orders of magnitude less than the accelerations induced by the thrust of nozzles and rotations of the space craft about the three axes. (The Coriolis force is sometimes the same order of magnitude as the centripetal acceleration but for simplicity this component is neglected for the 1/2 box model simulation. Variations of the acceleration magnitude with position in the stored fluid is also neglected for simplicity in the 1/2 box model simulation.)

There are five predominate types of flight modes which each have a typical "g" level and direction. They include

1) engine burns

2) attitude control maneuvers

3) passive thermal control (PTC)

4) attitude hold in translunar or transearth orbit

5) attitude hold in lunar orbit

The acceleration vector is parallel to the heater tube for type 1) operation. For the last three types of operation, the acceleration vector is predominantly perpendicular to the heater tube. Typical "g" levels in the last three are respectively 3×10^{-6} "g", 7×10^{-8} "g", and 5×10^{-7} "g".

Abrupt increases in "g" level ("g" spikes) can accompany
the use of the attitude control system. Then these "g"
directions are not necessarily perpendicular or parallel
to the heater tube.

The certainty with which the "g" level is known is esti-
mated to be better than a factor of 2 at 7×10^{-8} "g" and
better than a factor of 1.2 at 3×10^{-6} "g".

The energy input to the oxygen tank is composed of the
heater power and insulation heat leak. The latter never
exceeds   about ten percent of the former.   The estimation
of the heat leak is no more accurate than the estimate of
the oxygen flow rate but because it is a small fraction
of the total energy input and because the heater power is
known to about two percent, the overall energy input is
believed to be known to better than three percent.

The average cryogen density is obtained from the quantity
gauge and time integrals of the expulsion rate, initial
density, and container volume. The quantity is believed
to be known to about two percent.

The oxygen pressure is measured by a sensor whose output
is digitized in four psi intervals at the rate of about
one per second. The absolute value of pressure is known
to about 20 psi at 900 psia. The differences in pressure
are known to better than about four psi out of forty. A
similar situation exists in the absolute pressure measure-
ment of the surge tank.

If the difference of the container and surge tank pressure
depended only on the difference in these absolute pressure
measurements, considerable error would be possible. How-
ever, with normal crew compartment oxygen consumption
rates and no use of surge tank gas for other purposes,
the surge tank pressure must be the mean of the limit cycle
values of the container.

Thus a reference value of pressure is known and the surge
tank pressure gauge can be scaled accordingly. The flow

through the restrictor depends upon the pressure differential between the container and the surge tank. Since there is a flow meter between the crew compartment and the surge tank, a flow calibration of the restrictor is possible. The only time that the measurement of the flow to the surge tank requires the use of the restrictor calculation is when the surge tank pressure is different than the mean of the limit cycle values for the container. The estimate of the flow measurement accuracy is about 30 percent for the restrictor calculations. The mass flow rate to the fuel cells is known to about three percent which frequently is over half of the flow demand. The precision of the flow measurements then can be anything between three and thirty percent accurate depending upon the steadiness of the pressure in the surge tank and the crew compartment consumption rate.

The only other way to predict the average flow to the surge tank is with equations (A10) and (A11). The heat input, cryogen density, and changes in cryogen pressure can be used to estimate the average flow rate to the surge tank. However this procedure only is adequate when the stored cryogen is very recently stirred by the fans so that it is spatially isothermal.

It is hoped that the previous comments give some idea of the difficulty in obtaining accurate data which may be used to make predictions with the 1/2 box model. In spite of this situation, the predicted oxygen tank pressure history agrees   very favorably with the flight data. Because of the data uncertainty in some cases, good agreement may just be fortuitous. Some reduction of the ambiguity can be made by parametrically varying various of the data which are most suspect (e.g., "g" level and flow rate). The trends of such analysis can be used to gain confidence in the results and thus reduce the uncertainty.

The Comparison of Predictions and Flight Data

Two sets of data from the Apollo 12 flight have been reduced and summarized. Predictions for these cases have been made with the 1/2 box model. The comparisons are presented after some introductory discussion.

$\dot{P}_s/\dot{P}_e$ is defined as the ratio of the time derivative of the global pressure in cryogen which has a nonuniform and uniform time dependent temperature field respectively. For an ideal gas in which the compressibility and specific heats are constant, $\dot{P}_s/\dot{P}_e$ is unity whether or not temperature variations exist. In nonisothermal cryogen, at a density of about twice the critical, $\dot{P}_s/\dot{P}_e$ can approach a maximum value of about 16. As the density is reduced, $\dot{P}_s/\dot{P}_e$ approaches a value of unity. (Note that if $\dot{P}_s/\dot{P}_e$ is not unity, $\Delta P|_{max}$ can acquire nonzero values.) The actual value that $\dot{P}_s/\dot{P}_e$ acquires in finite difference calculations depends upon the resolution of the thermal boundary layer. With increasing acceleration level, natural convective mass rates increase near the heater surface and the heater surface temperature decreases. $\dot{P}_s/\dot{P}_e$ tends to unity for such heater temperature variation irrespective of the density of the cryogen. Coarse grid calculations of a thermal boundary layer with the 1/2 box model provide less boundary layer temperature variation and thus $\dot{P}_s/\dot{P}_e$ tends to be less than if fine grid calculations are used. Accordingly, prediction of the pressure history is very sensitive to thermal boundary layer resolution where $\dot{P}_s/\dot{P}_e$ potentially can deviate from unity which is the situation near and above the critical density.

At cryogen densities below and above the critical density, the accuracy of the predicted pressure history is sensitive to thermal boundary layer resolution but for another reason. The heater tube has significant thermal capacitance. The coarse grid calculations always predict excessive heater surface temperatures and as a result of the heater thermal capacitance excessively long pressurization cycles are predicted. Convergence studies are employed to estimate the effects of coarse grid calculations. This

means that the same problem is repeated for a number of different grid sizes.

For example, a 10 x 10, 20 x 10, 30 x 10, 40 x 10, 60 x 10, 80 x 10, 20 x 20 (the first and second integers are the number of computational cells in the x- and y- directions respectively), etc., grids may be used to predict a problem. By appropriately plotting the data, the convergence characteristics of some parameter of interest can be determined. If this procedure is used in a careful way beginning with the coarse grids first, estimates can be made as to how fine the grid must be to get the desired accuracy. This will be illustrated later.

The potential pressure decay ($\Delta P|_{max}$) may be defined as the amount the global pressure should decay when a cryogen is adiabatically restored to an isothermal state during which the fluid expulsion rate is zero. Truncation and conservation of energy errors can be delineated if the time integral of $\dot{P}_g$ is compared to the difference in the state of $\Delta P|_{max}$ for the boundary conditions of no boundary heating, no fluid expulsion, and no heater thermal capacitance. To illustrate such a comparison, two problems have been chosen and they differ only in the grid sizes which are a 6 x 6 and 12 x 12 and in the time step used after the "g" spike is initiated. The box has the dimensions of 2 x 2 x 1.187 feet for the height, width, and depth respectively. The initial density is about twice the critical density. Figure (5) shows the history of P_g and $\Delta P|_{max}$ of the 12 x 12 grid problem in which the fluid expulsion, wall heating, heater input, and acceleration level are nonzero for a period of time. The wall heating and heater input are chosen in order to generate an oscillating pressure history. The heater tube thermal capacitance is zero during the entire duration of the problem. The "g" level is chosen at 2 x 10^{-8} "g" so that the buoyantly driven mass rates are of the same order as the expulsion rate. At some later time, the "g" level is increased to 2 x 10^{-3} "g" in a time step and at the same time the expulsion rate and the boundary heating are set to zero. The "g" level increase causes a substantial increase in the buoyantly driven fluid velocity. As a result, the

74

high energy fluid which is concentrated in a glob near the
heater surface is rapidly stretched which substantially
enlarges it's surface area. This in turn enhances the
heat conduction and results in a rapid decrease in fluid
temperature differences. The sharp reduction in nonuniform
temperature field causes the global pressure to sharply
decay. The pressure decay rate is an order of magnitude
sharper than that which would have occurred had the "g"
level been unchanged during the course of the problem.
The time step is 30 seconds prior to the "g" spike and it
is reduced by

$$\Delta t = 0.4 \sqrt{\frac{(\Delta x, \Delta y)_{MIN}}{\beta}}$$

when the "g" spike occurs which yields a $\Delta t = 0.6977$ se-
conds and $\Delta t = 0.4933$ seconds for the respective problems.
The change in P_g of 41.0 and 49.3 corresponds to a change
in $\Delta P|_{max}$ of 42.5 and 49.6 respectively for the 6 x 6
and 12 x 12 grid problems. This yields respective differ-
ences in the actual and ideal decay changes of 2.8 and
0.3 psi for the respective problems. The reduction in
the error is entirely due to the time step reduction. Fur-
ther reduction in the time step after the "g" spike will
not significantly improve the result. This is due to the
fact that there is a small time dependent nonconservative
error in the energy convection terms. This error can be
virtually eliminated in the manner outlined in reference
(2).

Finally, the GEM has one other time related truncation
error which for the problems considered is trivial. The
algorithm exhibits a slight damping of kinetic energy and
this error may be eliminated with a nontrivial increase
in computer time. This consideration will be left to a
future paper.

As a rule, the truncation errors in time are well control-
led as the grid is refined. The significant errors for
fine grid calculations reduce to the definition of the
initial and boundary conditions. As has been mentioned
previously the mass expulsion rate is probably the most

inexactly known quantity. There are some other significant ones which are now discussed.

The elasticity factor (EF) for which a derivation is provided in the Appendix can be evaluated precisely except for term ($\rho_p V_p n / \rho_c V_c P$) which accounts for the external volume effect. Since there is no temperature sensor anywhere on the external plumbing, estimates of ρ_p and n (which is the reciprocal of the polytropic coefficient) must be made. (It is believed that ρ_p should be about 5 lb_m / ft^3 and n about 1.0. In this case, the magnitude of the effect of the external plumbing upon the elasticity factor is nearly negligible.) The elasticity factor is about one half at the high densities and rapidly approaches unity as the density is reduced to the critical value. It is unity for densities less than the critical value as well. Another difficulty in using the 1/2 box model arises in choosing the initial conditions for a given problem. As a rule, a uniform initial temperature field with a zero velocity field are the chosen initial conditions. The problems selected for analysis always have a fan cycle prior. Because the pressure response of the system appears to satisfy equations (A10) and (A11) of the Appendix, the isothermal assumptions appear to be warranted. But the zero velocity field prescription is certainly wrong except after the fluid motions from the fan cycle have decayed below those generated by the buoyant forces. Estimates of this decay time are made with fine grid calculations in which the initial field values of velocity are large. It has been found that less than about two hours are required to meet this condition at all fluid densities.

The treatment of the heater tube as a vertical flat plate in the 1/2 box model is believed to be wrong in one respect. Since the heater tube has only a few square inches of hole area through which high and low density fluid may flow, at low enough "g" levels some heated fluid can be trapped inside. This has the net effect of reducing the effective surface area for heat transfer. The "g" level at which the effective surface area is significantly reduced is at about 10^{-7} "g" or less.

The extremes of the surface area possible are

1) the total of the outside and the inside of the heater tube (about 1.1 ft^2)

2) the exterior of the portion of the tube which is wrapped with the heating elements (about 0.475 ft^2)

For the calculations presented, the value of 0.95 ft^2 is used and is twice the value of 2). This area certainly is a bit too large after some time period because of the restraint which the tube holes impose on the buoyantly driven flow and because the heater tube is not exactly isothermal along its length. (Evaluation of these two effects is currently under study.)

With these various reservations in mind, the two problems are now considered.

Two problems from Apollo 12 flight data were chosen for analysis because initial and boundary conditions could be reasonably assessed and because these problems exhibit the peculiar effects that the nonisothermal cryogen has upon the pressure history.

The 1/2 box model is assumed to be one foot wide, two feet high, and the depth is computed so that the volume is that of 1/2 of the oxygen tank which is 4.75 cubic feet.

The first flight problem of interest involves the prediction of the time required to raise the oxygen pressure about 33.5 psi in twelve minutes and forty seconds. The fan cycle occurred about eight hours prior to the time of interest. The pressure decayed steadily and the expulsion rate history could be found from equations (A10) and (A11). These values agreed well with those predicted from crew compartment and fuel cell flows. For this reason and since only heat leak was involved during the decay cycle, the system was believed to be essentially isothermal when the heater was activated, which is the beginning of the problem. The eight hour period was more than enough time for

the fluid velocity field to decay adequately so that the
zero field velocity prescription could be used at the be-
ginning of the prediction with the 1/2 box model. The
elasticity factor is about 0.97 so that the question of
how to evaluate the external volume effect is trivial.
Figure (6) shows the results of the 1/2 box model predic-
tions as a function of the grid size with and without the
heat tube capacitance of 0.07 BTU per degree Rankine. It
may be noted that the 60 x 10 and the 80 x 10 grid results
are nearly identical. Comparison of the velocity profiles
show that the boundary layer is well resolved by the 80 x
10 grid.

It is curious that the resolution is only weakly dependent
upon the number of cells in the y- direction. Figure (7)
shows the asymtotic estimate of the 1/2 box model predic-
tions. Figure (8) shows these asymtotic values replotted.
The agreement of the prediction and the flight data is
within about two percent which is better than would be
expected in view of the probable errors of the various
measurements. There are some interesting things to
note about the predictions.

The cryogenic oxygen density is slightly less than the
critical density. The average rate change of pressure is
about 15 percent larger than that which would occur for
isothermal cryogen. ($\dot{P}_s/\dot{P}_e$ is about 1.15 average value.
As a result, the adiabatic potential pressure decay ac-
quires a value of about 4 psi during the pressurization
stroke.) Also, the heater tube thermal capacitance is
shown to be a significant factor in the length of the
pressurization stroke. Thus without accounting for the
transient heater tube and thermal boundary layer inter-
action, the flight data could not well be predicted.

The 1/2 box model is used to simulate this problem again
but it differs from that shown in Figure (6) only in the
"g" level which is set at 4 x 10^{-7} "g". This lower "g"
level results in lower buoyantly driven mass rates by the
heater surface which results in a larger asymptotic

heater surface temperature. The asymptotic temperature differences between the heater surface and the bulk fluid is 230° R and 340° R for the problems at 2×10^{-6} "g" and 4×10^{-7} "g" respectively. Had the $\dot{P}_s/\dot{P}_e$ ratio remained the same for each of these problems, the latter problem would have had a pressurization stroke about a minute longer than that found for the former problem. This time increase is due entirely to the increased energy requirement of the heater tube. However, since the average value of $\dot{P}_s/\dot{P}_e$ for the latter problem is 1.23, the time increase caused by the heater tube capacitance effect is almost exactly offset and the resultant stroke length is only a few seconds longer. Since the reduction of the heater surface area to about a value of 0.7 ft^2 in the former problem would result in about the same asymptotic heater surface temperature, the pressurization stroke length would be almost exactly the same as that found in the latter problem. But since the latter and former problems yield almost identical stroke lengths, this problem is not suited to determining with precision the effective heater tube area. After examining the various errors and their effect on the results of the simulation, it is concluded that the heat tube thermal capacitance and the differential pressure measurement during the stroke are the primary parameters upon which the accuracy of the simulation depends. Since the agreement is excellent between the flight data and the prediction, it is concluded that whatever errors there are in these two parameters, they must be compensatory.

The second flight problem of interest examined in detail involves a high density problem in which the initial density is about twice the critical density. The elasticity factor is between 0.58 and 0.35 depending upon how the external volume effect is accounted for. The latter value assumes that the entire external plumbing volume is filled with cryogen which is at the density of the average of that of the stored fluid. From thermal studies of this plumbing system, such a condition is unlikely and it is probably the case that the entire volume contains near ambient oxygen. Since the process in the plumbing during the

pressure oscillations is probably isothermal, n is probably unity. With these assumptions the elastic factor is about 0.55 which means that the contribution from the external volume is only about five percent of the total.

The flow rate is time dependent and is modeled with the expression

$$\dot{m} = (0.755 + A + B)$$

where

$A = 0.1$ lb_m/hr when the heater is on

$A = 0$ lb_m/hr when the heater is off

$B = 0.17$ $(P_g - P_{surge})^{0.488}$ if $(P_g - P_{surge}) > 0$

$B = 0$ if $(P_g - P_{surge}) \leq 0$

where B is the flow through the orifice which is upstream of the surge tank. B is zero if the pressure difference $(P_g - P_{surge})$ is negative because a check valve in the line prevents reverse flow. P_{surge} is the surge tank pressure. The "g" level is time dependent and the values used in the simulation are shown in Figures (9, 10, and 11). Actually there are many more "g" spikes than indicated but these were deemed insignificant compared to those shown. Figures (9, 10, and 11) also show the end points of the pressure strokes for the flight data. The fan cycle occurred at about a ground elapse time (GET) of 4 hours and 27 minutes so the residual velocities should have been gone at the most by the time GET = 6:27. However examination of the length of the strokes show that within about 40 minutes the predominate effects of the fan cycle had dissipated. Thus the stroke length is then relatively fixed and is modified predominantly by the "g" spikes. Note how sharp the pressure change is with the "g" spikes but that no substantial change in fluid pressure occurs until the "g" level increased to 10^{-3} "g". A dramatic decay of fluid pressure then ensues and an enlarged view of this event is shown in

Figure (11). The fans are turned on before the course of
the "g" spike induced pressure decay stroke is run. It
appears however from the slope of the decay curve prior to
the fan cycle, that virtually all of the potential for
pressure decay would have been absorbed. Thus properly
interspersed "g" spikes of sufficient magnitude could be
used to provide the same function as the fans, that of
stirring the stored cryogen so that it's temperature field
is for practical purposes isothermal.

Attempts to simulate the pressure history of this problem
have begun but are not yet complete. As a consequence,
only preliminary results from 1/2 box model studies are
presented. Between GET = 4:29 and 4:41, the decay cycle
as noted before, involves a cryogen whose temperature field
is isothermal, but time dependent. The end points of this
pressure cycle have been predicted to better than twenty
seconds in eleven minutes with the 1/2 box model. The same
result is obtained with the equations (A10 and A11). So
that the remainder of the four hour simulation could be put
on one plot, this decay stroke is omitted from any display.
Figure (12) shows a pressure trace for a 60 x 10 grid in
which the previously given flow rate equation was not em-
ployed. (The pressure trace for the included flow equa-
tion could not be prepared in time for this publication.
With some exceptions the average flows are about the same
and for discussion purposes it will serve to illustrate
the important features of the simulation.) A convergence
study shows that the 60 x 10 grid almost adequately resolves
the thermal boundary layer during the periods between GET =
4:41 and 5:53 and between 6:40 and 8:33. During, and some
time after the "g" spikes, the thermal boundary layer is
not well resolved. It is estimated that about at least a
150 x 40 grid would be required during this period. (With
existing computers, this degree of resolution is impracti-
cal. However, a variable mesh grid system is being de-
veloped which hopefully will permit resolution which is
more nearly adequate.)

It should be noted that the length of the pressurization
stroke in Figure (12) is short sooner than shown in Figure

(6). This is believed to be due to the difference in the
initial conditions which has been already noted. At GET
5:41, the stroke lengths are about the same and this may
be noted by examining Figure (13) which shows the plot of
the pressurization stroke length versus the number of grid
points. (The flight data is also shown.). The asymptotic
value is believed to be almost attained with the 80 x 10
grid. (The variable mesh program may provide the tool
necessary for the practical verification of this belief.)
If so, the agreement between the simulation and the flight
data is good.

The stroke length of the pressurization cycle shown in
Figure (13) is about three times less than that predicted
for a cryogen whose temperatire field is isothermal, but
time dependent. If the heater tube thermal capacitance is
zero in the 1/2 box model, the stroke length is about
fifteen times less than that predicted for a cryogen whose
temperature field is isothermal, but time dependent. The
elasticity factor and expulsion mass rate inaccuracies
can, at most, only affect the pressurization stroke length
by about a factor of two. Thus accurate simulation of the
transient thermal boundary layer and heater tube tempera-
ture are the most important considerations in predicting
the pressurization stroke length.

With regard to the simulation of the "g" spikes, it may be
noted that there are several qualitative and quantitative
resemblences with the flight data. This is true of several
of the small "g" spikes and the large "g" spike event which
occurs at the end of the simulation. This latter event has
been enlarged and displayed in Figure (14). The magnitude
of the pressure decay is substantially attenuated by the
heat which is derived from the rapid cooling of the heater
tube. (Convergence studies are currently being performed
for this "g" spike event in order to attempt to gain quan-
titative data on the grid sizes required for adequate
resolution.) The obvious disagreements between the flight
data and the simulation are believed to be due to

   1) since simulated strokes are not in phase with flight

"g" data, the "g" spikes occur at different relative positions in the stroke than is shown for the flight data

2) the geometry of the heater tube probably plays some part

3) the grid is certainly too coarse

Further studies of this problem will hopefully provide the information which is necessary to delineate the importance of each of these considerations.

In spite of the preliminary nature of the data thus far acquired for this flight problem, the results to date are very encouraging, enough so that further work is warranted.

Conclusions

The methodology of the General Elliptic Method for the simulation of time dependent single-phase cryogenic flow has been presented. A brief description of the Apollo 12 single-phase oxygen storage system has been presented along with some discussion of the elements which are considered for the reduction of flight data. The 1/2 box model in which the boundary conditions used to simulate the cryogenic oxygen flow processes of the Apollo 12 oxygen tank has been presented. Mention has been made of some of the difficulties which have arisen in obtaining accurate quanitative data from the 1/2 box model and the flight data. In spite of these difficulties, the comparisons of the predictions and the flight data are shown to be good.

It is recommended that further application of the 1/2 box model be made to predict flight system response as the flight data becomes available. Assessment of the deficiencies and capabilities of the 1/2 box model would then be possible for a wide range of flight conditions. If the overall results are reasonably favorable, prediction of the oxygen tank pressure history for future missions could then

be undertaken with a confidence well beyond that pre-
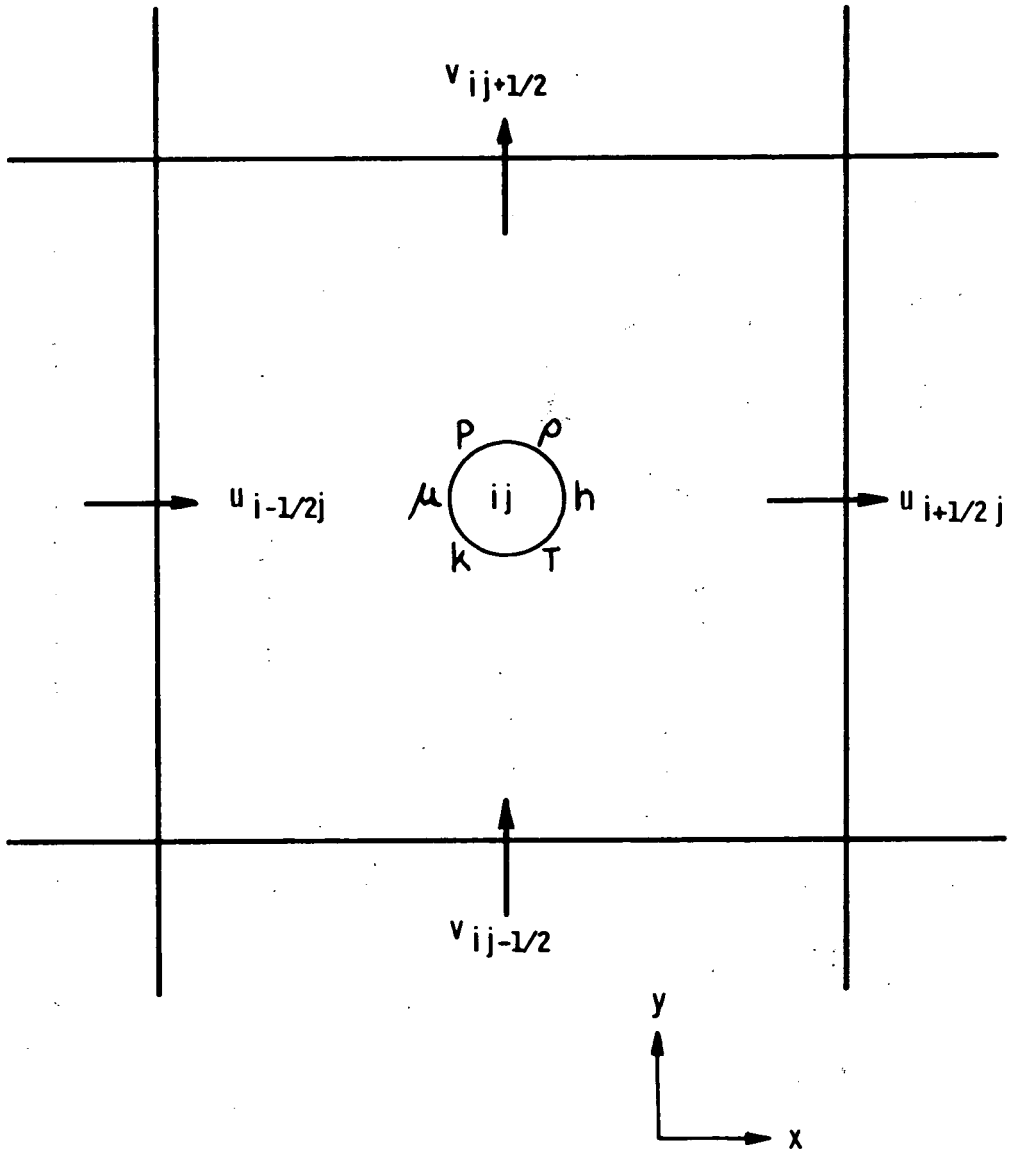viously available.
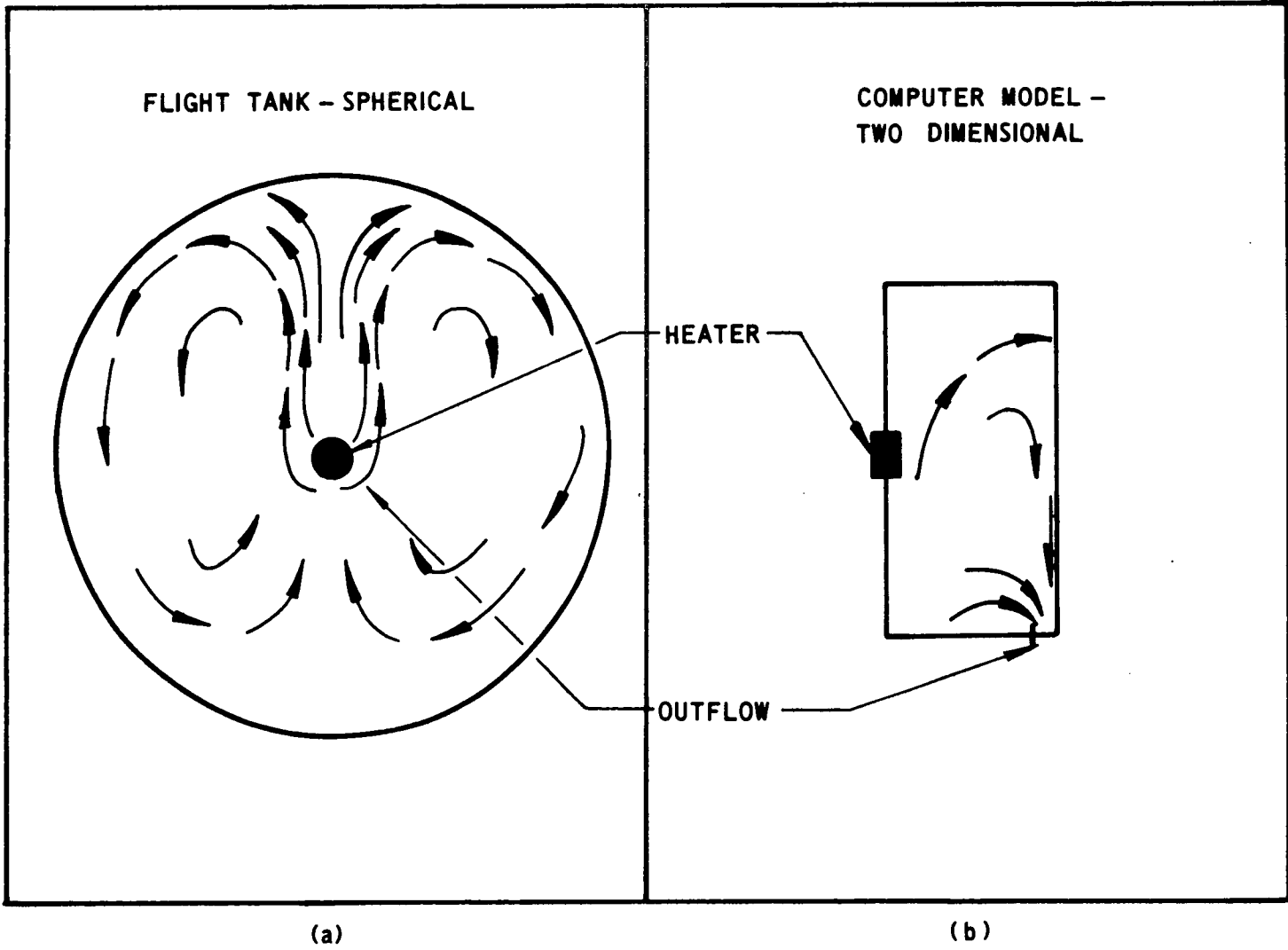
Figure 1. TYPICAL CROSS SECTION OF A COMPUTATIONAL CELL

85

FLIGHT TANK – SPHERICAL

COMPUTER MODEL –
TWO DIMENSIONAL

HEATER

OUTFLOW

(a)

(b)
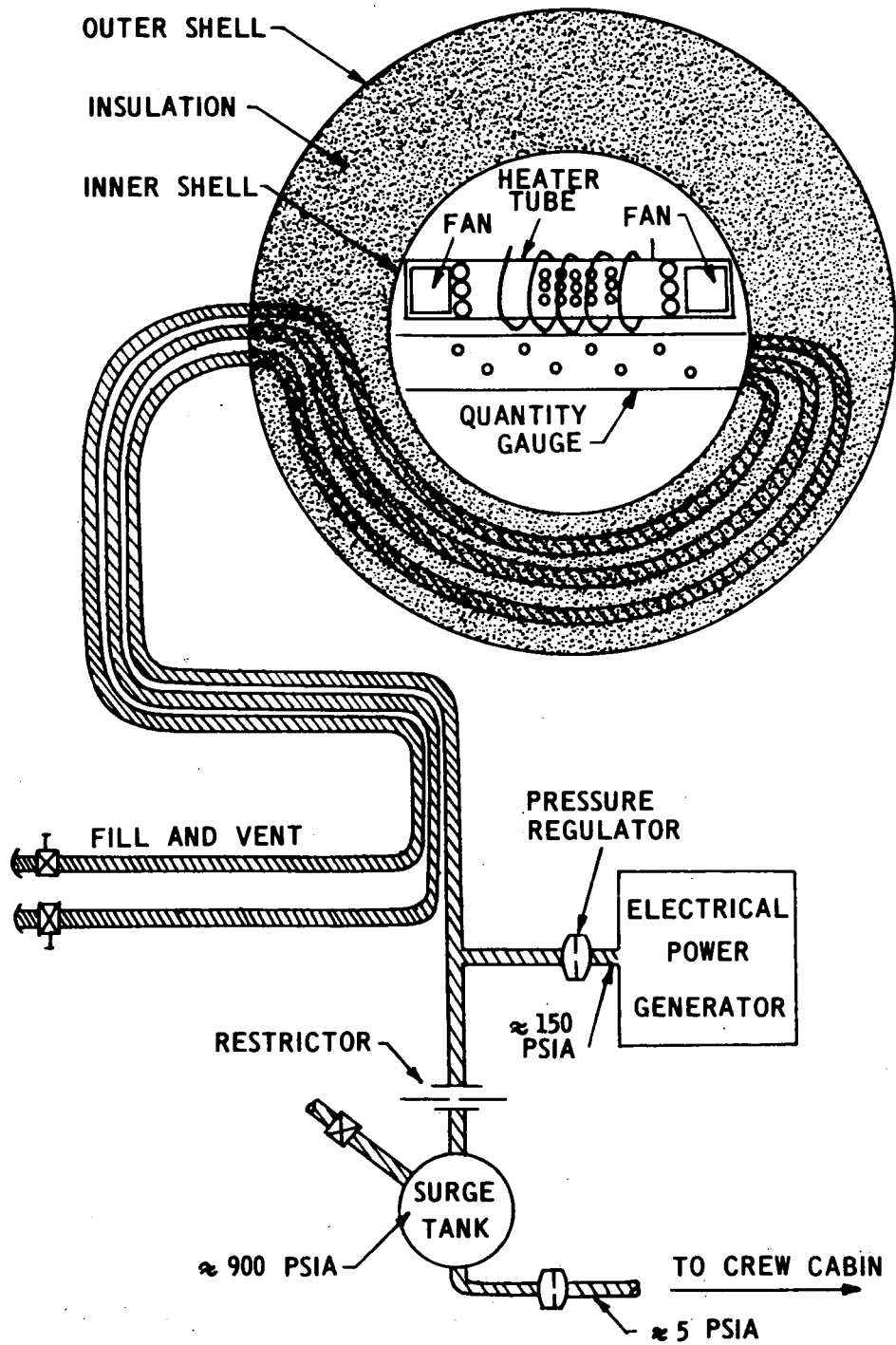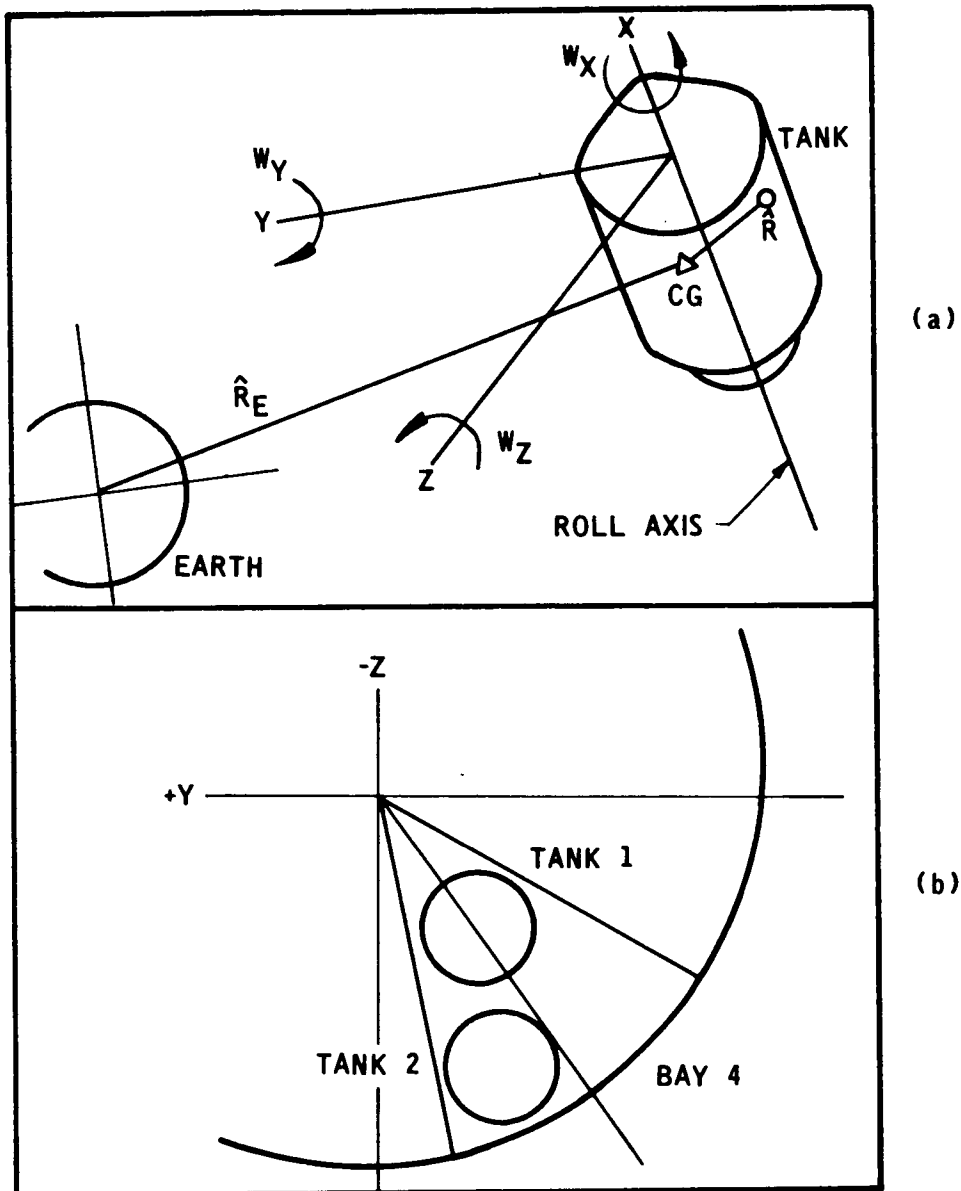
Figure 2. ANALYTICAL APPROACH

Figure 3. APOLLO 12 OXYGEN TANK AND SUPPLY SYSTEM SCHEMATIC

ACCELERATION DUE TO ROTATION:

$$A_{ROT} = (\hat{\dot{W}} \times \hat{R}) + (\hat{W} \times \hat{W} \times \hat{R})$$

ACCELERATION DUE TO GRAVITY GRADIENT:

$$A_{GG} = \frac{-2M_E G \; \hat{R}_E \cdot \hat{R}}{\hat{R}_E^{\,4}} \; \frac{\hat{R}_E}{|\hat{R}_E|} \qquad A_{TOTAL} = A_{ROT} + A_{GG}$$

SOLAR PRESSURE AND SOLAR WIND ARE NEGLECTED

Figure 4. O_2 TANK ACCELERATIONS
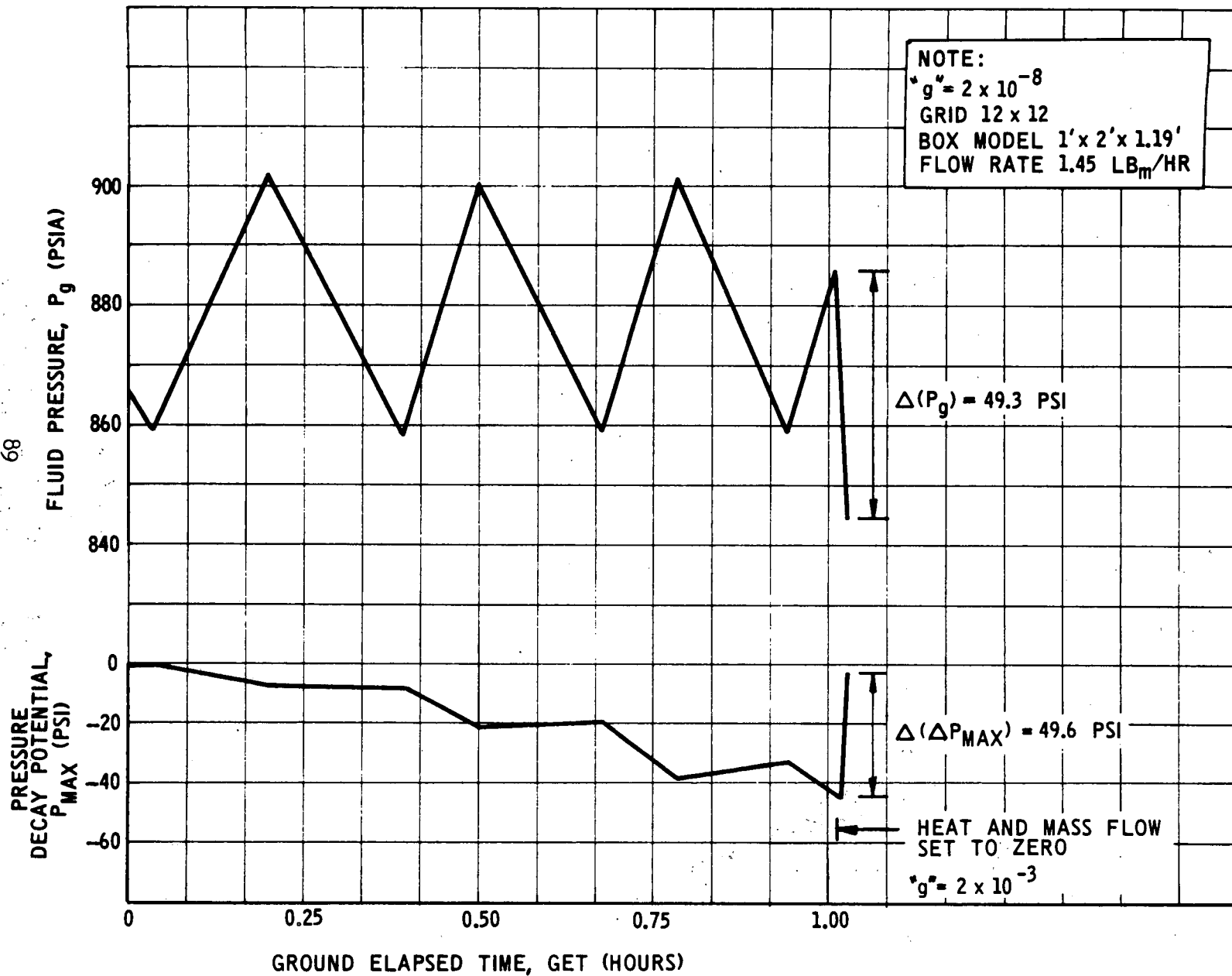
Figure 5. "g" SPIKE SIMULATION
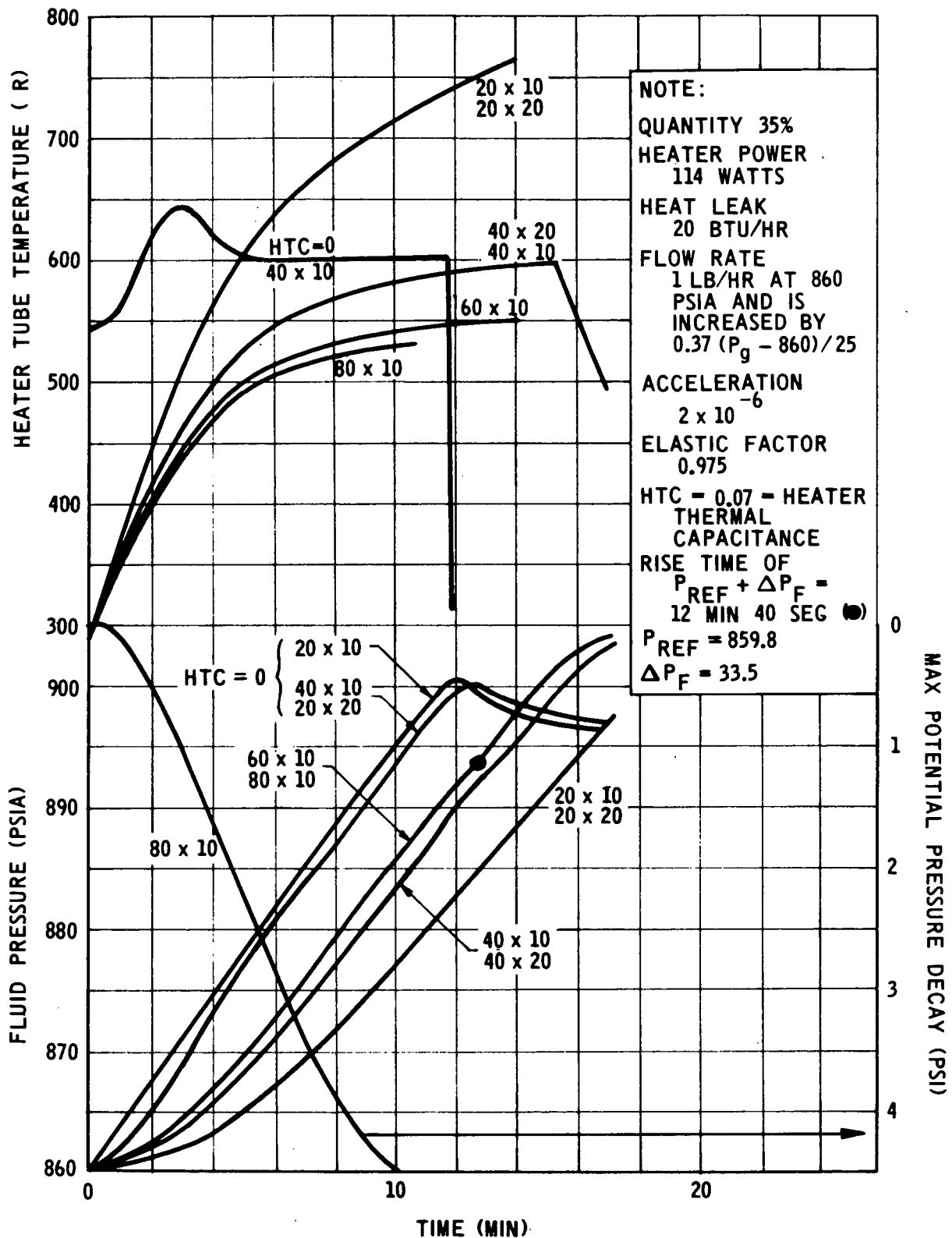
Figure 6.   APOLLO 12 OXYGEN TANK No. 1
PASSIVE THERMAL CONTROL MODE

90
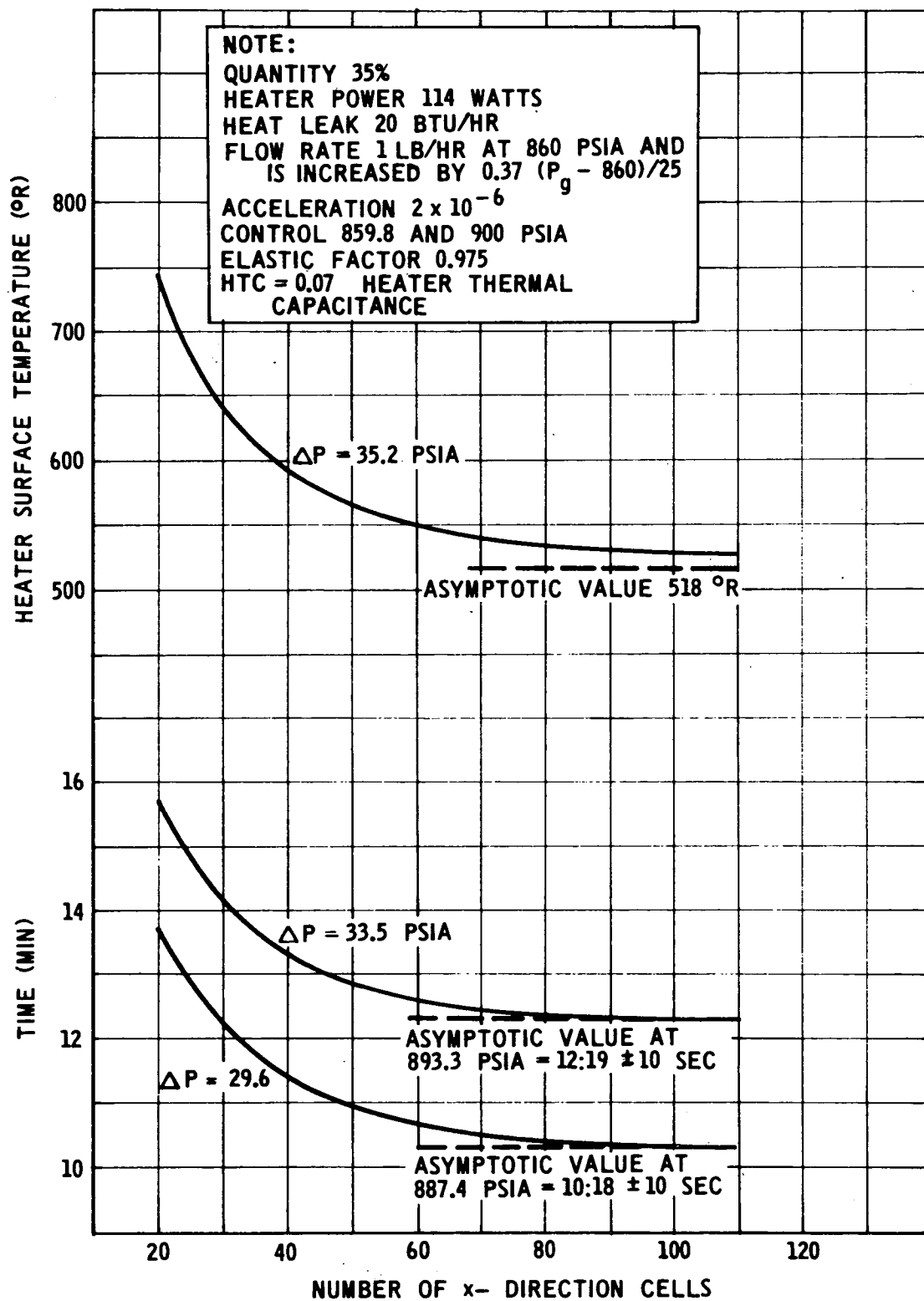
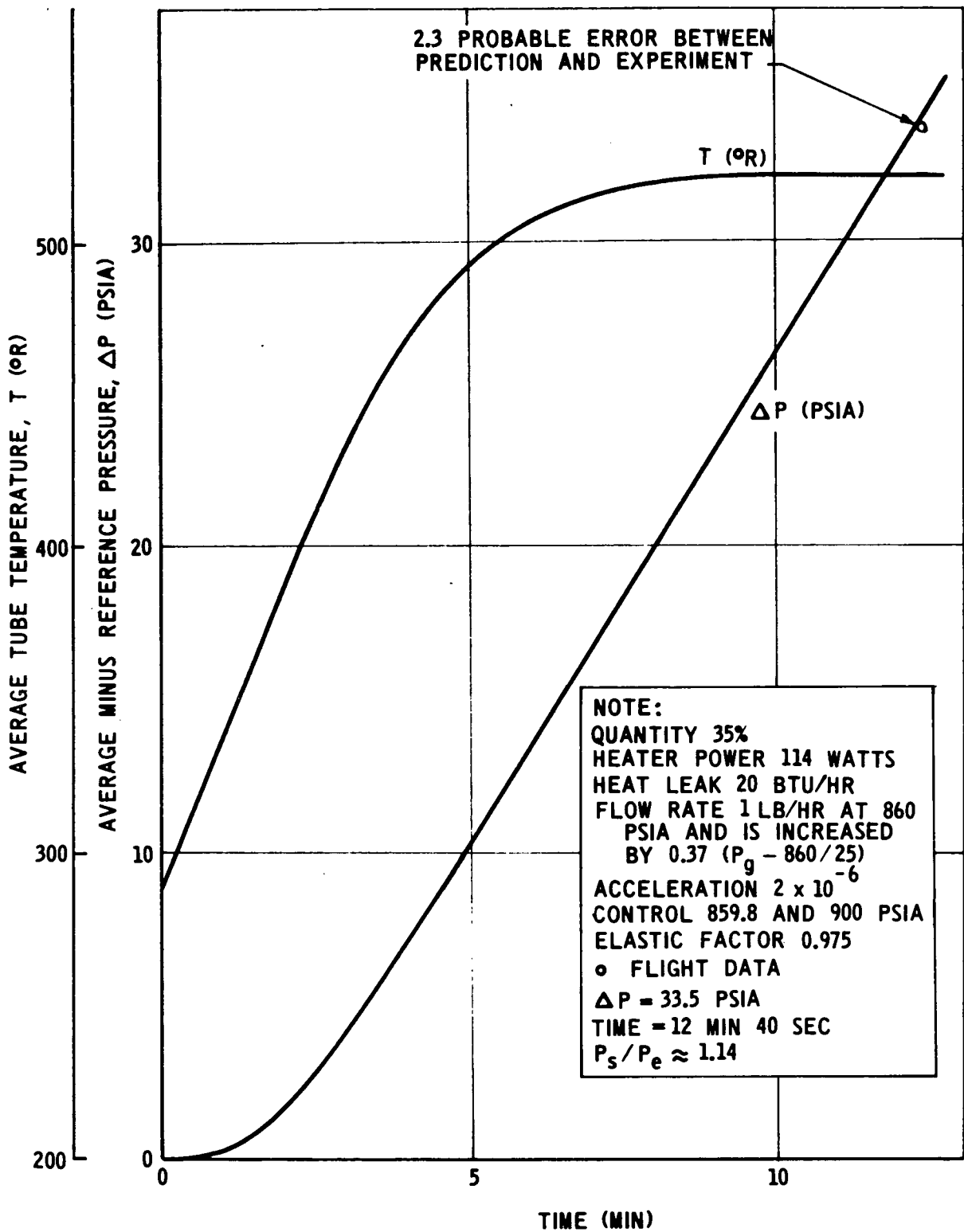Figure 7.   APOLLO 12 OXYGEN TANK No. 1
PASSIVE THERMAL CONTROL MODE

91

Figure 8. APOLLO 12 OXYGEN TANK No. 1
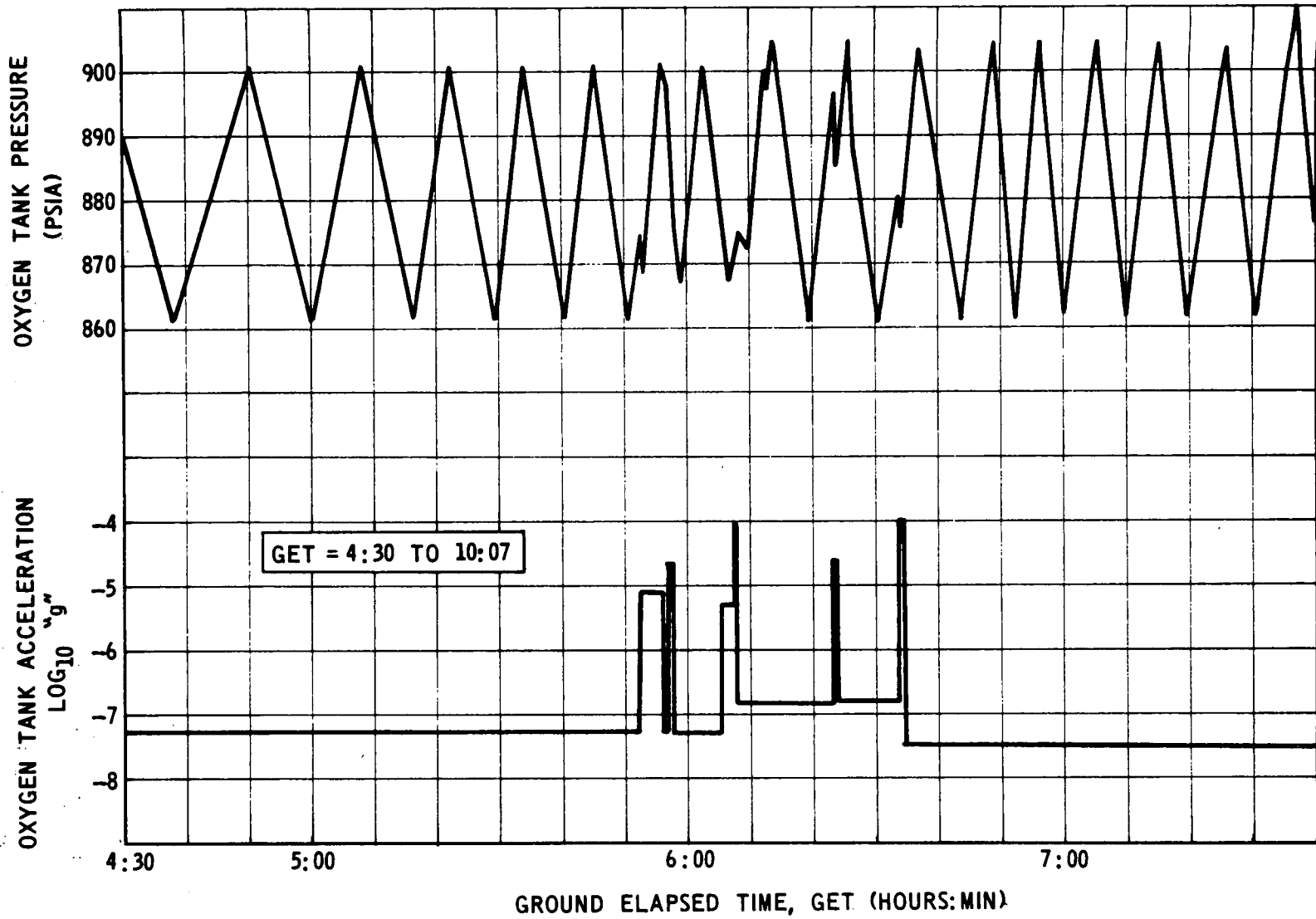PASSIVE THERMAL CONTROL MODE
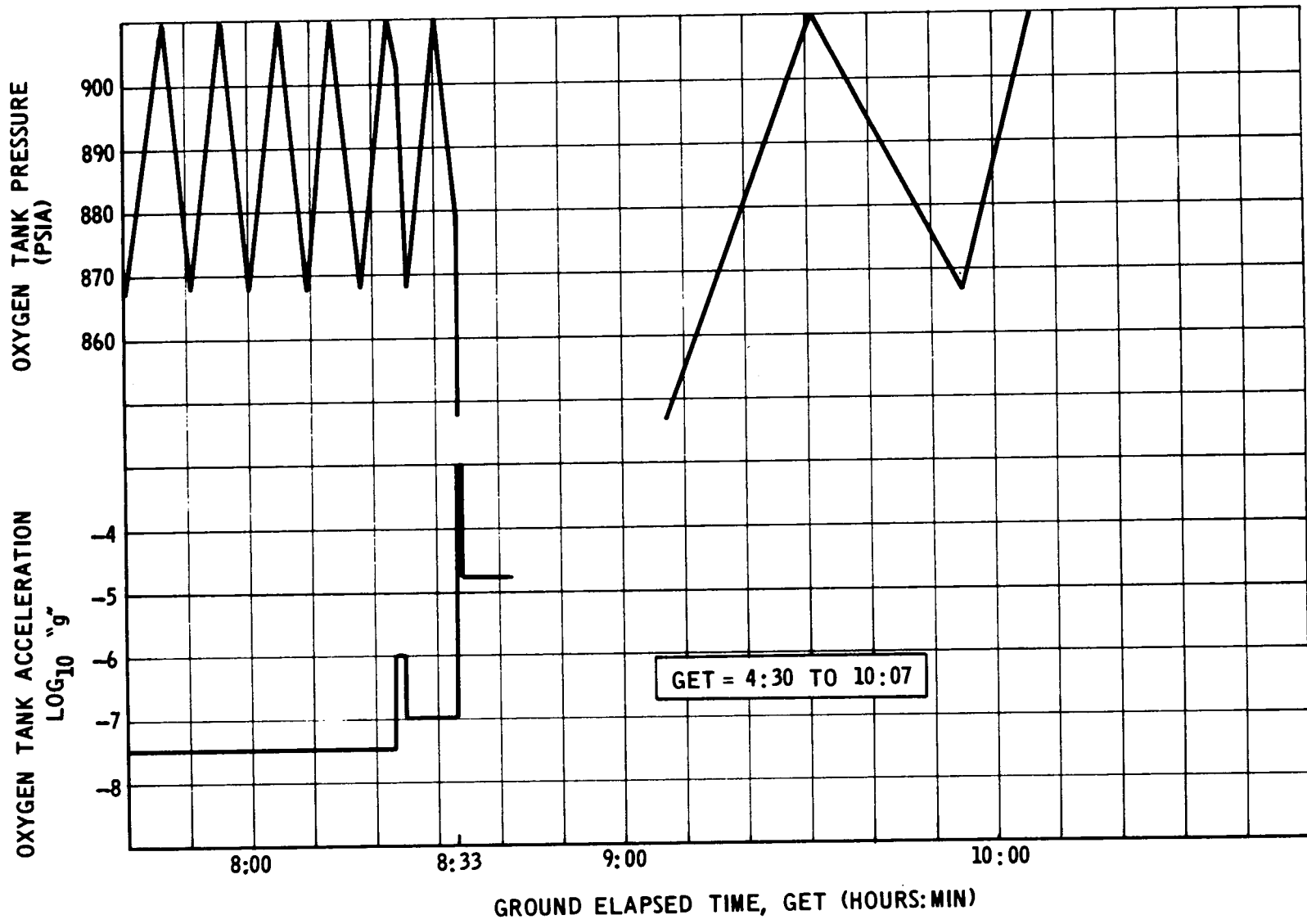
92

Figure 9. APOLLO 12 FLIGHT DATA — ATTITUDE HOLD

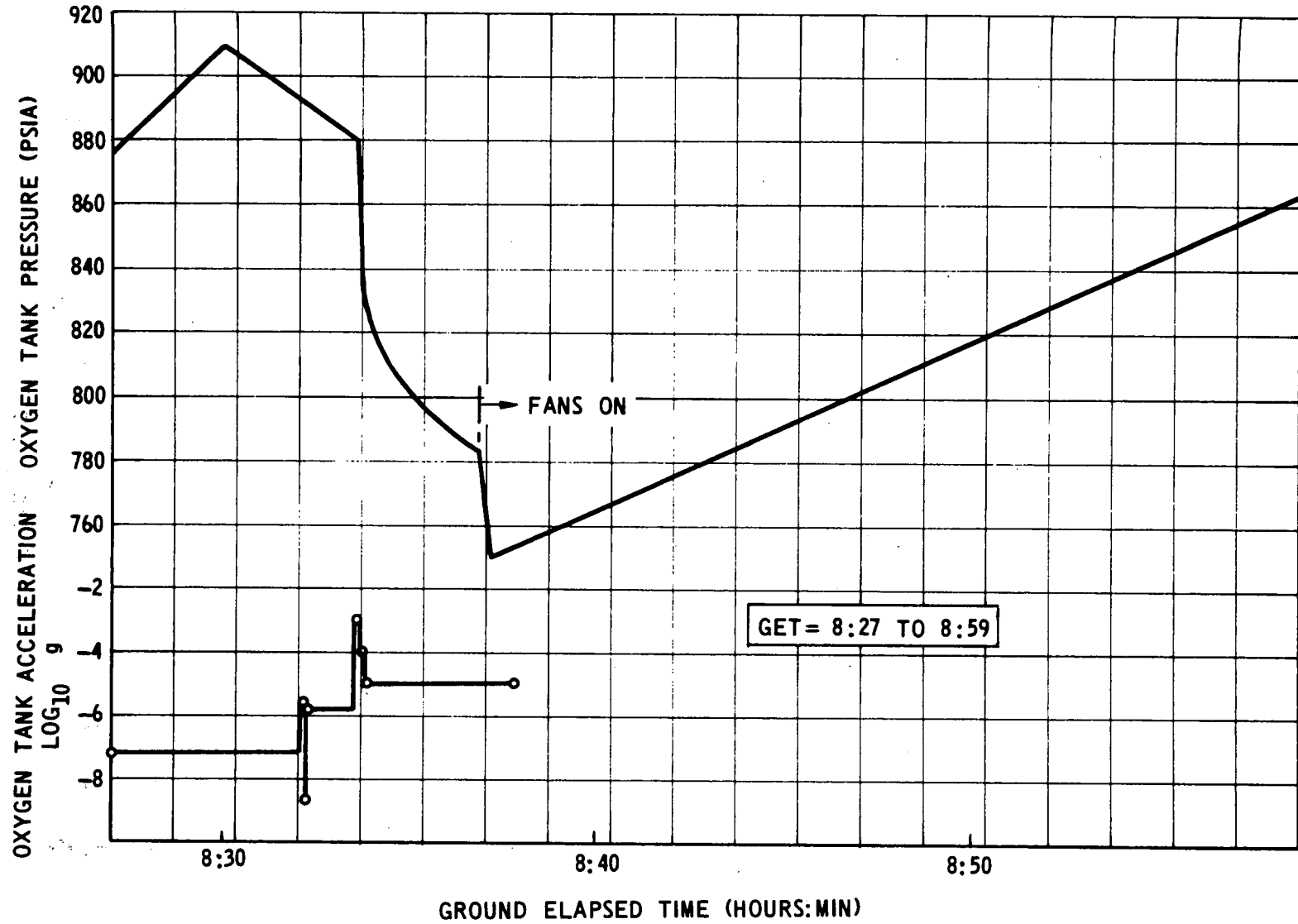Figure 10. APOLLO 12 FLIGHT DATA — ATTITUDE HOLD

94

Figure 11.   APOLLO 12 FLIGHT DATA – ATTITUDE HOLD

QUANTITY 95 PERCENT   HEATER POWER 114 WATTS
ACCELERATION 7X10 -8G   HEATER AREA   0.95 FT. SQ.
GRID SIZE 60 X 10   THERMAL MASS 0.07 BTU/DEG R
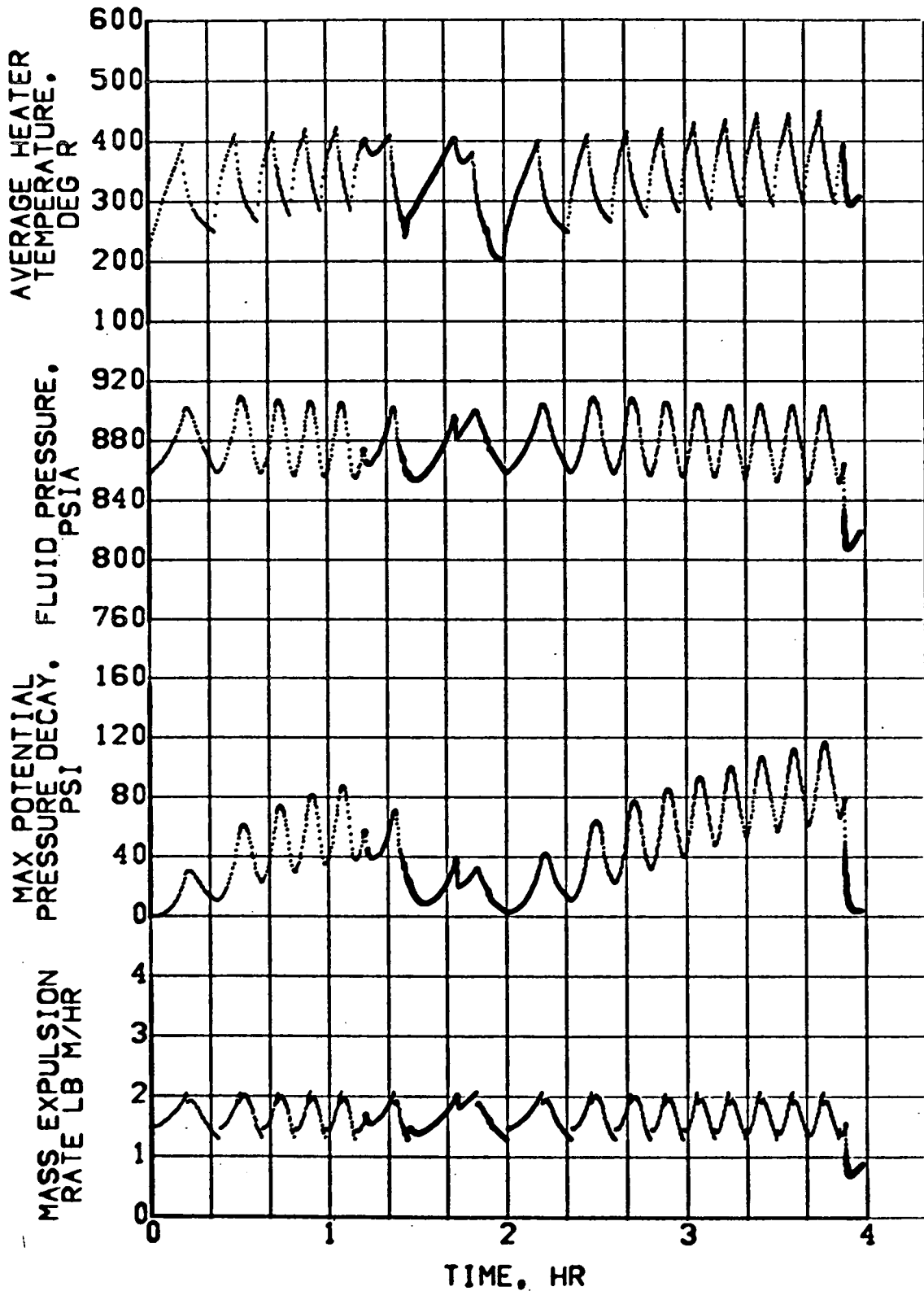
Figure 12. APOLLO 12 SIMULATION

NOTE:

GRID   60 x 10
SIMULATION FROM GET
       4:41 TO 8:37
"g" SPIKE 4×10^{-8}
       INCREASE TO 1×10^{-3}

TANK PRESSURE (PSIA)

940

900

860

820

780

740

MODEL SIMULATION

FLIGHT DATA

8:31   8:32   8:33   8:34   8:35   8:36

GROUND ELAPSED TIME, GET (HOURS:MIN)
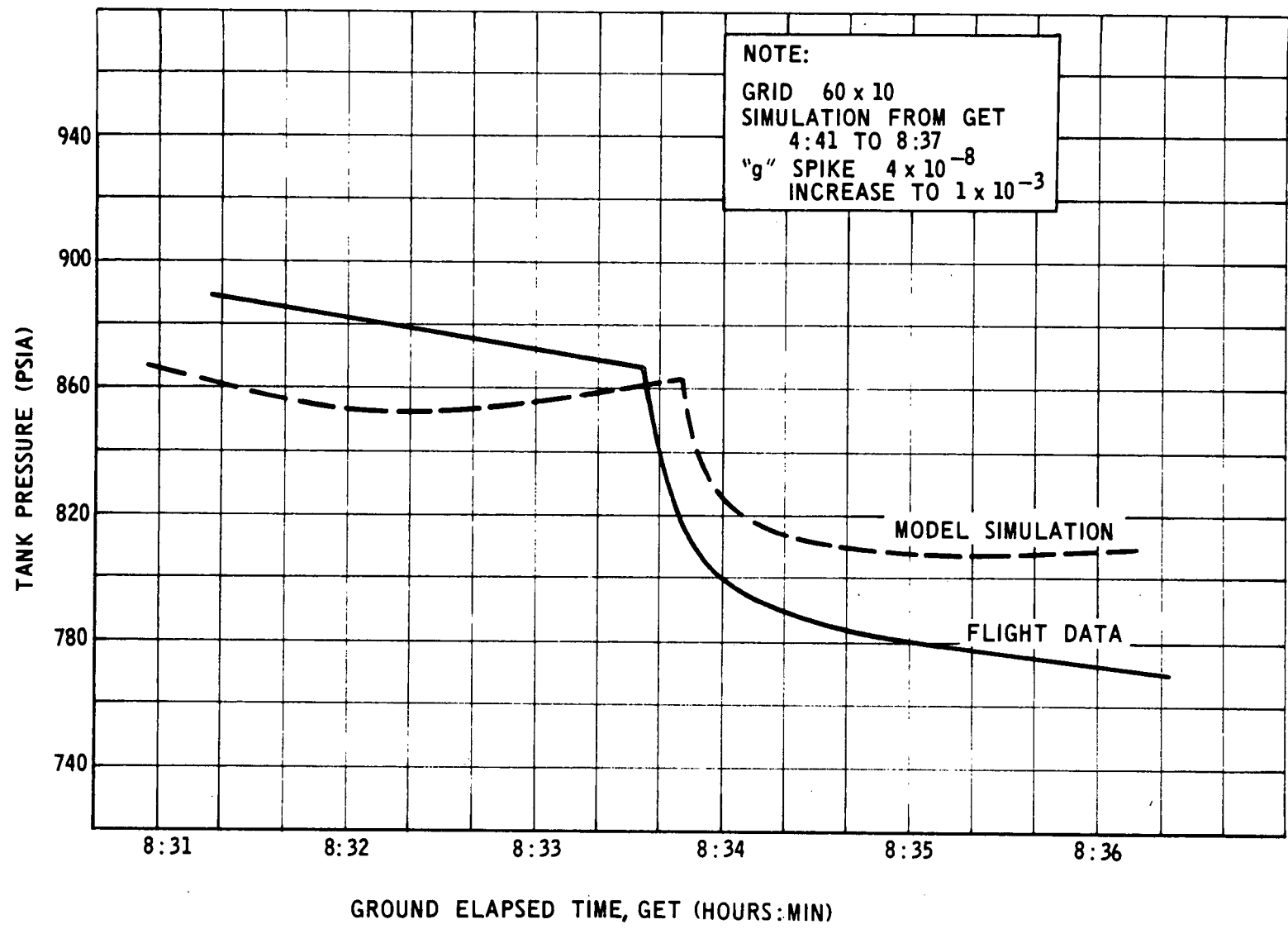
Figure 13.   APOLLO 12 "g" SPIKE SIMULATION

97

NOTE:
QUANTITY 95%
HEATER POWER 114 WATTS
HEAT LEAK 14.5 BTU/HR
FLOW SHOWN IN FIGURE 13
ACCELERATION 7×10^{-8}
CONTROL 860 TO 900 PSIA
ELASTIC FACTOR 0.397

FLIGHT DATA

AVERAGE PRESSURIZATION STROKE RATE (PSI/MIN)

x- DIRECTION CELLS
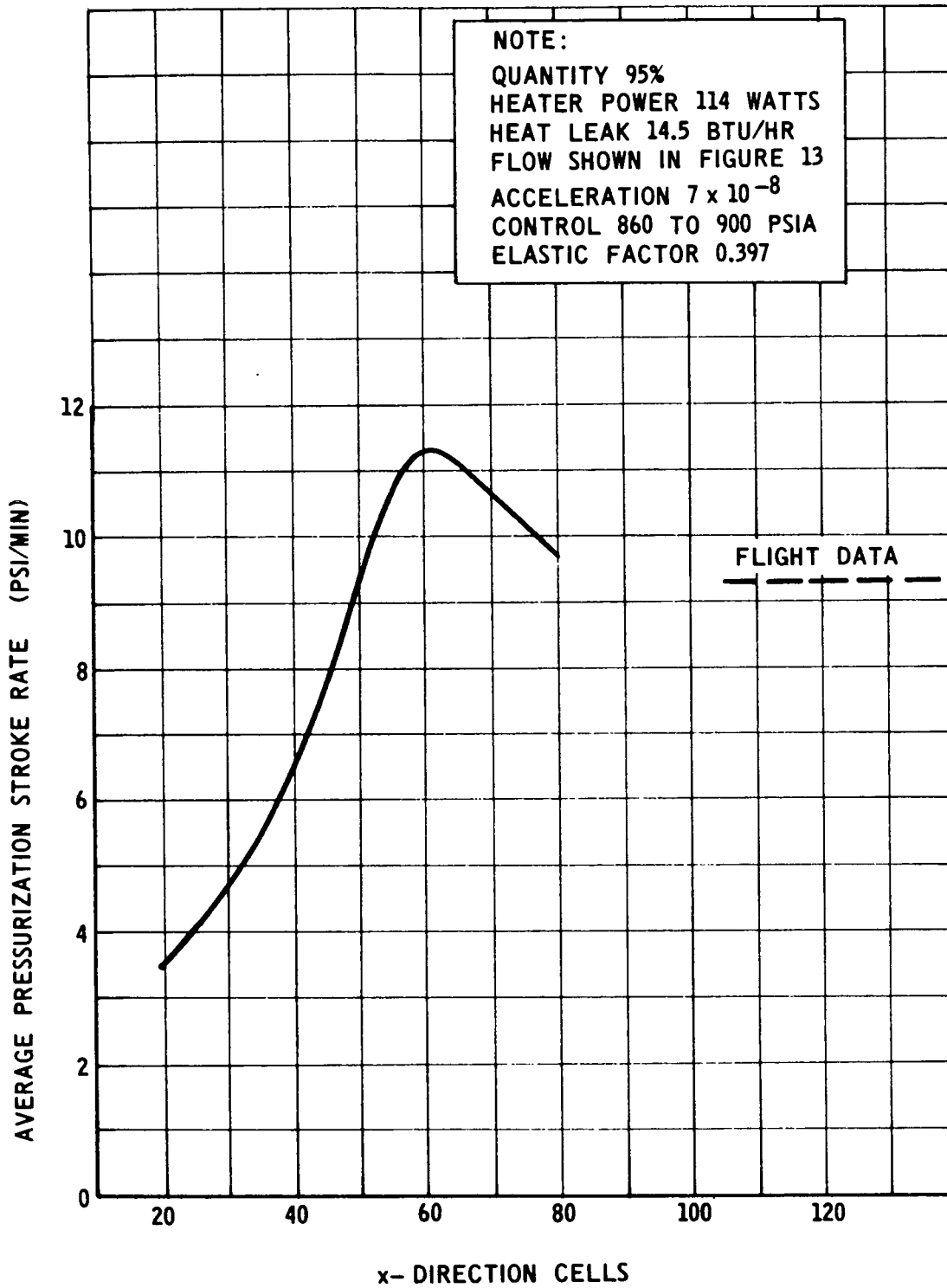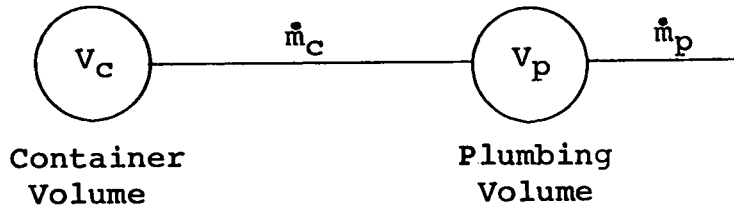
Figure 14. APOLLO PRESSURE STROKE RATE VS GRID SIZE

98

The Derivation of the Elastic Factor (EF) for the Spherical Container and the External Plumbing

Container Volume   Plumbing Volume

System Schematic

Assumptions:

1) The volume (V_c) is enclosed by a thin walled elastic spherical container with a response of

$$\left(\frac{1}{V_c}\right) \frac{dV}{dP}\bigg|_c = \frac{3r(1-\sigma)}{2bE}$$

where

r = container radius

σ = Poisson's ratio

b = container thickness

E = Young's modulus

2) The plumbing volumes (V_p) are rigid $(dV/dP)|_p = 0$ and contain a compressible gas with a response $P = Z \rho RT$ in which the rate change of compressibility (Z) with respect to the pressure (P) is zero $(dZ/dP = 0)$.

3) The time (t) derivative of pressure is a constant for all the fluid in the system $(dP/dt)|_c = (dP/dt)/_p$.

4) The enthalpy and temperature properties are only functions of the pressure and the density for the stored fluid.

Now define

$$\theta \equiv -\rho \left.\frac{\partial h}{\partial P}\right|_\rho \quad , \quad \phi \equiv \left.\frac{\partial P}{\partial(\rho e)}\right|_\rho \quad , \quad h \equiv e + \frac{P}{\rho} \quad ,$$

$$\frac{dM_c}{dt} = -\dot{m}_c \quad , \quad \frac{dM_p}{dt} = \dot{m}_c - \dot{m}_p \quad , \quad \frac{d\rho}{dt} \equiv \dot{\rho} \quad ,$$

$$\frac{dP}{dt} \equiv \dot{P} \quad , \quad \rho_c \equiv \left(\frac{M}{V}\right)_c \quad , \quad \rho_p \equiv \left(\frac{M}{V}\right)_p$$

The result of time differentiation of ρ_c and ρ_p after invoking assumption 2) and some appropriation definitions are

$$\dot{\rho}_c = \frac{1}{V_c}\left.\frac{dM}{dt}\right|_c - \frac{M_c}{V_c^2}\frac{dV_c}{dt} = -\frac{\dot{m}_c}{V_c} - \frac{\rho_c}{V_c}\frac{dV_c}{dt} \tag{A1}$$

$$\dot{\rho}_p = \frac{\dot{m}_c - \dot{m}_p}{V_p} \tag{A2}$$

The energy balance for V_c is

$$\frac{d}{dt}(\rho e V)_c = \dot{Q}_c - \dot{m}_c h_c - P\frac{dV_c}{dt} \tag{A3}$$

100

The subscript c is now dropped from (A3) until some inter-
mediate manipulations are complete. Since

$$\rho e = \rho e \, (P, \rho)$$

$$\frac{d(\rho e)}{dt} = \dot{\rho} \left[\frac{\partial(\rho e)}{\partial \rho} \bigg|_P \right] + \left[\frac{\partial(\rho e)}{\partial P} \bigg|_\rho \right] \dot{P}$$

$$= \dot{\rho} \left[\frac{\partial \rho(h - \frac{P}{\rho})}{\partial \rho} \bigg|_P \right] + \frac{\dot{P}}{\Phi} = \dot{\rho}(h - \theta) + \frac{\dot{P}}{\Phi} \qquad (A4)$$

Now by substitution eliminate d (ρe)/dt from (A3) and
(A4) and combine the result with (Al) and an appropriate
definition to yield

$$\dot{P} \frac{V}{\Phi} + \frac{dV}{dt} (\rho \theta) = \dot{Q} - \dot{m} \, \theta \qquad (A5)$$

Now by the chain rule

$$\frac{dV}{dt} = \frac{dV}{dP} \frac{dP}{dt}$$

and combined with (A5) with the subscript c restored is

$$\dot{P}_C = (\frac{\Phi}{V})_C \, (\dot{Q}_C - \dot{m}_C \, \theta_C) \, (EF) \qquad (A6)$$

where

$$(EF) \equiv \frac{1}{1 + (\rho \Phi \theta)_C \, (\frac{dV}{dP})_C} \qquad (A7)$$

Invoking assumption (1), (A7) may be written as

$$(\mathrm{EF}) = \frac{1}{1 + (\rho\phi\theta)_c \, \frac{3r(1-\sigma)}{2b\mathcal{E}}} \tag{A8}$$

The state equation $P = ZR\rho T$ with the appropriate definition may be written as

$$P = \left(ZRM \frac{T}{V} \right)_p$$

and may be differentiated with respect to V_p and after some alegraic manipulation is

$$\left(V \frac{dV}{dP} \right)_p = \left[-\frac{ZMRT}{VP^2} + \frac{MRT}{VP} \frac{dZ}{dP} + \frac{ZR}{VP} \left(T \frac{dM}{dt} \frac{dt}{dP} + M \frac{dT}{dP} \right) \right]_p$$

and after assumptions (3) and (4) and the definition of $d\rho_p/dt$ is employed, simplifies to

$$\dot{P}_p = \frac{(\dot{m}_c - \dot{m}_p) \, P_p}{(\rho V)_p} \tag{A9}$$

(A6), (A8), and (A9) may be combined to yield

$$\dot{P}_c = \left(\frac{Q}{V} \right)_c \left(\dot{Q}_c - \dot{m}_p \, \theta_c \right) (\mathrm{EF}) \tag{A10}$$

where

$$(\mathrm{EF}) \equiv \frac{1}{1 + (\rho\phi\theta)_c \left[\frac{3r(1-\sigma)}{2b\mathcal{E}} + \frac{(\rho V)_p \, (n)}{(\rho V)_c \, P} \right]} \tag{A11}$$

where $n = 1$

It can additionally be shown that for a polytropic heating $1 \geqslant n \geqslant C_v/C_p$ where n is unity for the isothermal case and C_v/C_p for the isentropic limit.

102